Abundances, masses, and weak-lensing mass profiles of galaxy clusters as a function of richness and luminosity in ΛCDM cosmologies

Stefan Hilbert[1,2]⋆ and Simon D. M. White[2]

[1] *Argelander-Institut für Astronomie, Auf dem Hügel 71, 53121 Bonn, Germany*
[2] *Max-Planck-Institut für Astrophysik,Karl-Schwarzschild-Straße 1, 85741 Garching, Germany*

28 October 2009

ABSTRACT
We test the concordance ΛCDM cosmology by comparing predictions for the mean properties of galaxy clusters to observations. We use high-resolution *N*-body simulations of cosmic structure formation and semi-analytic models (SAMs) of galaxy formation to compute the abundance, mean density profile, and mass of galaxy clusters as a function of richness and luminosity, and we compare these predictions to observations of clusters in the Sloan Digital Sky Survey (SDSS) maxBCG catalogue. We discuss the scatter in the mass-richness relation, the reconstruction of the cluster mass function from the mass-richness relation, and fits to the weak-lensing cluster mass profiles. The impact of cosmological parameters on the predictions is investigated by comparing results from galaxy models based on the Millennium Simulation (MS) and another WMAP1 simulation to those from a WMAP3 simulation. We find that the simulated weak-lensing mass profiles and the observed profiles of the SDSS maxBCG clusters agree well in shape and amplitude. The mass-richness relations in the simulations are close to the observed relation, with differences $\lesssim 30\%$. The MS and WMAP1 simulations yield cluster abundances similar to those observed, whereas abundances in the WMAP3 simulation are 2-3 times lower. The differences in cluster abundance, mass, and density amplitude between the simulations and the observations can be attributed to differences in the underlying cosmological parameters, in particular the power spectrum normalisation σ_8. Better agreement between predictions and observations should be reached with a normalisation $0.722 < \sigma_8 < 0.9$ (probably closer to the upper value), i.e. between the values underlying the two simulation sets.

Key words: galaxies: general – galaxies: clusters: general – large-scale structure of the Universe – gravitational lensing – cosmology: theory – methods: numerical

1 INTRODUCTION

Clusters of galaxies are a powerful probe of astrophysics and cosmology (Voit 2005). For example, the cluster mass function is very sensitive to the cosmic mean matter density, to the initial fluctuation amplitude (Press and Schechter 1974; Frenk et al. 1990; Eke et al. 1996; Sheth and Tormen 1999) and to dark energy dynamics (Bartelmann et al. 2006; Grossi and Springel 2009; Francis et al. 2009). It can be predicted to high accuracy by numerical simulations (Jenkins et al. 2001; Warren et al. 2006; Lukić et al. 2007).

However, the masses of galaxy clusters cannot be observed directly. Thus one either needs to infer the masses of observed clusters from some more directly observable cluster property, requiring accurate knowledge of the observable-mass relation and its scatter, or one must directly compare observed and predicted cluster abundance as a function of such observables. These include the X-ray luminosity and temperature of the intracluster gas (Borgani et al. 2001; Reiprich and Böhringer 2002; Stanek et al. 2006; Piffaretti and Valdarnini 2008; Vikhlinin et al. 2009), the number and velocity dispersion of the cluster galaxies (Zwicky 1937; Rines et al. 2003; Kochanek et al. 2003; Becker et al. 2007), the number of giant arcs (Bartelmann et al. 1998; Wambsganss et al. 2004; Fedeli et al. 2008), the weak-lensing signal (Tyson et al. 1990; Cypriano et al. 2004; Hoekstra 2007; Johnston et al. 2007b; Reyes et al. 2008), and the Sunyaev-Zel'dovich signal induced by the cluster (White et al. 2002; Schulz and White 2003; Bonaldi et al. 2007; Staniszewski et al. 2009).

⋆ shilbert@astro.uni-bonn.de

Predictions for many cluster observables (e.g. the X-ray luminosity or the cluster richness) and for their relation to the cluster mass require modelling of astrophysical processes such as gas cooling and galaxy formation. Although inaccuracies in such astrophysical models are an unpleasant source of uncertainty for cosmological parameter estimation, they mean that comprehensive observations of clusters can be used to constrain cosmological parameters and models for cluster/galaxy evolution simultaneously.

The largest sample of observed galaxy clusters currently available is the maxBCG cluster catalogue (Koester et al. 2007a), This was extracted from the Sloan Digital Sky Survey (SDSS)[1] using maxBCG, an optical cluster-finding algorithm (Koester et al. 2007b). Constraints on the scatter in the velocity dispersion-richness relation and the mass-richness relation of these clusters have been derived from cluster X-ray and galaxy velocity dispersion observations (Becker et al. 2007; Rozo et al. 2009a). Weak-lensing measurements of average cluster mass profiles have also been used to calibrate the mass-richness relation, the mass-optical luminosity relation, and mass-to-light ratio profiles of the maxBCG clusters (Sheldon et al. 2009a,b; Johnston et al. 2007b; Reyes et al. 2008). These data provide significant constraints on cosmological parameters (Rozo et al. 2009b).

In this work, we investigate how well physically based models for galaxy formation in a ΛCDM universe can reproduce the observed relations of cluster richness and luminosity to other cluster properties, most notably mass. We also investigate what information on cosmological parameters and galaxy evolution can be obtained by comparing model predictions to observation. We use the Millennium Simulation (Springel et al. 2005) and two smaller N-body simulations of cosmic structure formation (Wang et al. 2008) in conjunction with semi-analytic models of galaxy evolution (De Lucia and Blaizot 2007; Wang et al. 2008) to create mock catalogues of galaxy clusters selected similarly to the maxBCG catalogue. We compute cluster abundances, average cluster masses, and weak-lensing mass profiles as a function of cluster richness and luminosity, and we compare these to observational results for the SDSS maxBCG sample. In addition, we investigate the scatter in the mass-richness relation, and we discuss how well one can recover the cluster mass function and the weak-lensing mass profiles from the richness-binned cluster abundances and mean masses.

The semi-analytic galaxy models used here couple star formation in galaxies to the properties of the evolving dark matter halo distribution in which the galaxies live. The models have been adjusted to be consistent with various observations, e.g. the luminosities, stellar masses, morphologies, gas contents and correlations of galaxies at low redshift, but they have not been tuned to match the properties of rich clusters. The comparison to observations provided here is thus a direct test of these models and their description of the physical processes relevant for galaxy formation. This contrasts with halo occupation distribution models (Cooray and Sheth 2002), where the galaxy populations of clusters are adjusted to fit observation without considering in detail how they could have been built up by physical processes within the evolving dark matter distribution.

Table 1. The cosmological parameters at redshift 0 for the three simulations used in this study. The parameters are: the baryon density Ω_{b}, the matter density Ω_{M}, and the energy density of the cosmological constant Ω_{Λ} (in units of the critical density), the Hubble constant h (in units of $100\,\mathrm{km\,s^{-1}Mpc^{-1}}$), the primordial spectral index n and the normalisation parameter σ_8 for the linear density power spectrum.

	MS & WMAP1	WMAP3
Ω_{b}	0.045	0.04
Ω_{M}	0.25	0.226
Ω_{Λ}	0.75	0.774
h	0.73	0.743
n	1	0.947
σ_8	0.9	0.722

Our paper is organised as follows. We discuss the N-body simulations and galaxy models, as well as our methods for creating the simulated cluster samples from them in Sec. 2. Results for our simulated cluster samples and a comparison to observation are presented in Sec. 3. Our paper concludes with a summary and discussion in Sec. 4.

2   METHODS

We use cosmological N-body simulations to analyse the matter distribution in and around galaxy clusters in two different ΛCDM cosmologies. We infer the properties of the galaxies in the clusters from model galaxy catalogues generated by applying semi-analytic galaxy formation models to halo assembly trees generated from the outputs of the N-body simulations. We then compute richness and luminosity estimates for clusters in the model galaxy catalogues taking into account several observational features of optical cluster-finding algorithms, in particular maxBCG by Koester et al. (2007b).

2.1   The N-body simulations

Our study is based on three different N-body simulations: the Millennium Simulation (MS) by Springel et al. (2005), and two smaller simulations WMAP1 and WMAP3 by Wang et al. (2008).[2] The simulations assume a flat ΛCDM cosmology with parameters given in Table 1. Both the MS and the WMAP1 simulation use a parameter set that was derived by combining the WMAP 1st-year results (Spergel et al. 2003) with results from the 2dFGRS (Colless et al. 2003). The WMAP3 simulation employs cosmological parameters that are consistent with data from the WMAP 3rd-year release, the Cosmic Background Imager, and the Very Small Array (Spergel et al. 2007), with a bias towards values differing from those used for the other two simulations.

The most prominent differences between the two sets of cosmological parameters are the normalisation parameter σ_8 and the spectral index n for the density power spectrum: The MS and the WMAP1 simulation assume $\sigma_8 = 0.9$ and $n = 1$, whereas the WMAP3 simulation assumes lower values $\sigma_8 =$

Table 2. Numerical parameters for the three simulations used in this study. The parameters are: the comoving cube size L, the particle number n_p, the particle mass m_p, and the effective force softening length ϵ.

	MS	WMAP1	WMAP3
L [h^{-1}Mpc]	500	125	125
n_p	2160^3	560^3	560^3
m_p [h^{-1}M$_\odot$]	8.6×10^8	8.6×10^8	7.8×10^8
ϵ [h^{-1}kpc]	5	5	5

0.722 and $n = 0.94$. Hence, there is less power on small scales in the matter power spectrum of the WMAP3 simulation than in the MS and the WMAP1 simulation. This results in a substantial delay in structure formation and less massive collapsed structures at any given redshift in the WMAP3 simulation.

The simulations were run using a parallel TreePM version of GADGET2 (Springel 2005). The numerical parameters of the simulations are listed in Table 2. The main difference between the MS and the WMAP simulations is the simulation box size. The large volume of the MS provides us with a large sample of galaxies and galaxy clusters with statistical errors comparable to the 'cosmic variance' errors of the SDSS maxBCG sample. The smaller WMAP simulations differ in their cosmological parameters, but share the same numerical parameters and initial conditions.[3] This reduces the influence of sampling noise when comparing results between the WMAP simulations and allows us to study the influence of cosmology on our results.

For each simulation, the particle data were stored on disk at 64 output times. These snapshots contain information on dark-matter halos, which have been identified running a friend-of-friend (FOF) group finding algorithm on the set of simulation particles. The halos were later decomposed into subhalos using SUBFIND (Springel et al. 2001) to identify gravitationally self-bound locally overdense regions. The most massive subhalo, called the main subhalo, typically contains 90% of the FOF halo mass and shares its centre. Detailed merging history trees of all self-bound dark-matter subhalos were then computed. The resulting merger trees were used as input for the semi-analytic models discussed in the following section.

2.2 The semi-analytic galaxy models

We use semi-analytic galaxy formation models from the Munich family (Kauffmann et al. 1999; Springel et al. 2001; De Lucia et al. 2004; Springel et al. 2005; Croton et al. 2006; De Lucia and Blaizot 2007) to set the optical properties of galaxies in the N-body simulations. These semi-analytic models assume that galaxies form from gas that accumulates in the centre of each dark-matter subhalo in the simulation. Star formation in each galaxy is coupled to its subhalo properties via simple prescriptions for gas cooling, star formation,

chemical enrichment and feedback from supernova and central black holes (AGNs), as well as for merging of galaxies once their dark matter subhalos have merged. Certain parameters quantifying the efficiency of these processes can be adjusted in order to maximise agreement of the results with observation.

For the MS, we use the publicly available galaxy catalogue[4] that was generated using the galaxy model described in De Lucia and Blaizot (2007). This MS model reproduces various observed relations for galaxies, in particular the observed luminosity, colour, gas content and morphology distributions (Croton et al. 2006; De Lucia et al. 2006; Kitzbichler and White 2007) and the observed two-point correlation functions (Springel et al. 2005; Kitzbichler and White 2007).

The galaxy model of De Lucia and Blaizot (2007) has been applied by Wang et al. (2008) to the WMAP1 simulation using the same set of efficiency parameters. As expected, this gives similarly good agreement with observations as for the MS. Here, we will use these model galaxies, which we refer to below as the WMAP1-A model, for the WMAP1 simulation.

Wang et al. (2008) also applied the galaxy modelling technique of De Lucia and Blaizot (2007) to the WMAP3 simulation, but with two slightly different sets of efficiency parameters. One, which we call WMAP3-B here, employs the same star formation efficiency as the WMAP1-A model, but lower supernova and AGN feedback efficiencies. The other model, called WMAP3-C in the following, employs a higher star-formation efficiency but also higher feedback efficiencies. Both the WMAP3-B and the WMAP3-C model show good agreement with low-redshift galaxy observations, e.g. of the galaxy luminosity function and the galaxy clustering (Wang et al. 2008). In the following, we will consider both models for the WMAP3 simulation.

2.3 The ridgeline galaxies

Optical cluster finding algorithms such as maxBCG (Koester et al. 2007b) locate galaxy clusters by searching for local overdensities of E/S0 ridgeline galaxies in angular and redshift space. These galaxies are common in known clusters, and they are relatively easy to find, since many of them are bright and their observed colours are strongly correlated with luminosity and redshift. Because of their small scatter in colour, a narrow search range in colour can be chosen at each redshift. This narrow search range forces one to know the mean ridgeline colours rather accurately. Accurate mean ridgeline colours are also important for accurately quantifying the ridgeline galaxy content of the clusters.

Although the semi-analytic models can reproduce many of the observed properties of galaxies, there are still some discrepancies. In particular, the models do not reproduce the colours of passively evolving galaxies to the degree required for a direct application of the ridgeline colour-redshift relation used for the maxBCG catalogue (see, e.g., Weinmann et al. 2006, for possible reasons). We therefore 'measure' the mean ridgeline colours of model galaxies as a function of redshift: We roughly identify the mean colour of the ridgeline galaxies in the colour-magnitude diagram (where

---

[3] Their initial density fields are identical except for small amplitude adjustments needed to reproduce the correct matter power spectra.

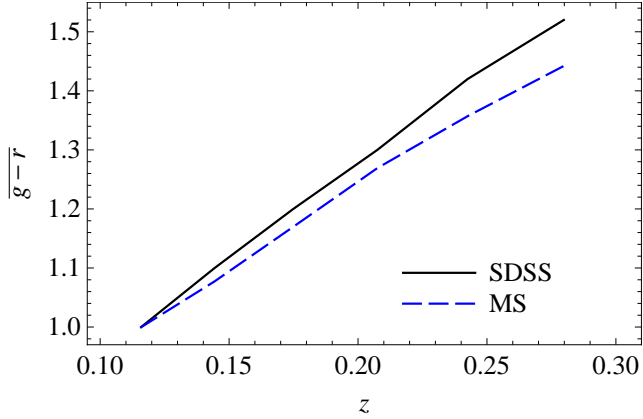[4] http://www.mpa-garching.mpg.de/Millennium

Figure 1. The mean colour $\overline{g-r}(z)$ of the ridgeline galaxies as a function of redshift z for the galaxy model of De Lucia and Blaizot (2007) in the MS compared to the mean colour-redshift relation for the ridgeline galaxies in the SDSS (Koester et al. 2007b).

the ridgeline population induces a visible overdensity among the bright galaxies with colours close to the observed mean ridgeline colour). We then fit a Gaussian with mean $\bar{x}$ and variance σ^2 to the distribution of galaxy colours in a region around our initial colour guess. We repeat the fit considering all galaxies with absolute i-band magnitudes $M_i \leqslant -20$ and colours in the range $\bar{x} \pm 3\sigma$ until $\bar{x}$ converges.[5]

The resulting mean ridgeline colours for model galaxies in the MS as a function of redshift is compared to the corresponding relation for SDSS galaxies in Fig. 1. The mean ridgeline colours of the model are close the observed ridgeline colours at low redshift, but they deviate significantly at higher redshift. The measured ridgeline width $\sigma_{g-r} \approx 0.05$ for all considered galaxy models and redshifts, which is in agreement with observations (Koester et al. 2007b). The measured width in $(r-i)$-colour $\sigma_{r-i} \approx 0.03$, which is smaller than the observed value $\sigma_{r-i} = 0.06$.

Following the maxBCG observational procedure, we consider $g-r$ and $r-i$ colours to identify ridgeline galaxies in our simulations. For each simulation snapshot with redshift $0.1 \leqslant z \leqslant 0.3$, we select all objects in our semi-analytic galaxy catalogues whose $g-r$ and $r-i$ values are both within 2σ of the mean ridgeline colours. As mean colours, we take the values measured from the simulations. For the ridgeline width σ, we take the observed values $\sigma_{g-r} = 0.05$ and $\sigma_{r-i} = 0.06$ (Koester et al. 2007b).

Besides colour, galaxy brightness is used to select ridgeline galaxies. We thus further select from all model galaxies surviving the colour selection those with apparent observer-frame i-band magnitude $i^{\mathrm{obs}} \leqslant i_{\mathrm{lim}}^{\mathrm{obs}}$. Here, we employ the same magnitude limit $i_{\mathrm{lim}}^{\mathrm{obs}}$ as Koester et al. (2007b) (B. Koester, private communication). This magnitude limit corresponds to an absolute rest-frame magnitude limit $M_i^{\mathrm{rest}} \approx -20.25 + 5\log_{10} h \approx -20.9$ for the cosmologies considered here.

2.4 The galaxy clusters

We identify galaxy clusters in the simulations with dark matter halos found by the FOF algorithm. From the simulation data stored on disk, we obtain for each such halo (hence cluster candidate) the positions of the centre, the virial radius $R_{200}^{\mathrm{crit/mean}}$ (i.e. the radius of the largest sphere enclosing $200\times$ the critical/mean density) and the mass $M_{200}^{\mathrm{crit/mean}}$ (i.e. the mass enclosed within $R_{200}^{\mathrm{crit/mean}}$).

The semi-analytic galaxy models provide us with information about the galaxies associated with each dark matter halo. For each halo, we measure the total number $N_{\mathrm{int}}^{\mathrm{gal}}$ of associated ridgeline galaxies selected as described in the preceding section. In addition, we count the number of ridgeline galaxies $N_{1\mathrm{Mpc}}^{\mathrm{gal}}$ within a physical radius of $1h^{-1}$ Mpc in projection along a simulation box axis. The result is used to compute the "observationally defined" radius $R_{200}^{\mathrm{gal}} = 0.156(N_{1\mathrm{Mpc}}^{\mathrm{gal}})^{0.6} h^{-1}$ Mpc (see Hansen et al. 2005; Koester et al. 2007b). We then calculate a scaled galaxy richness N_{200}^{gal} by counting all ridgeline galaxies within a projected radius R_{200}^{gal}. A cluster luminosity L_{200}^{gal} is then computed by summing the i-band luminosities of all ridgeline galaxies within R_{200}^{gal}. These procedures mimic closely those employed to estimate richnesses and luminosities for the real maxBCG catalogue.

To improve statistics, we perform the measurements of the projected quantities $N_{1\mathrm{Mpc}}^{\mathrm{gal}}$, R_{200}^{gal}, N_{200}^{gal}, and L_{200}^{gal} along all three simulation box axes. Each projection is treated as an individual cluster in the subsequent analysis. For the computation of cluster densities, the resulting triplication of clusters is taken into account by assuming a three times larger simulation volume.

Several effects hamper a direct comparison between observed clusters and our simulated clusters at the stage described so far. Here, we will not take into account fragmentation, but we do correct for contamination of the observational data by foreground and background galaxies.[6] Using spectroscopic data, Koester et al. (2007a) found that roughly 16% of the galaxies identified by maxBCG as cluster ridgeline galaxies are, in fact, projections. We include such projections in our simulated clusters in a very simple way, by randomly duplicating about 19% of the ridgeline galaxies. As a result, our model clusters appear to be contaminated at the 16% level.

We also consider the effect of misidentifying the cluster centre. For each cluster in the simulations, we calculate galaxy numbers, radii, etc. not only using the 'true' centre, but also using the position of the second-most massive subhalo as 'apparent' centre. The resulting distribution of projected offsets R_s between 'true' and 'apparent' centre is shown in Fig. 2 for the MS. The distribution can be approximated by a two-dimensional Gaussian distribution with

$$\mathrm{pdf}(R_s) = \frac{R_s}{\sigma_s^2} \exp\left(-\frac{R_s^2}{2\sigma_s^2}\right) \qquad (1)$$

and $\sigma_s = 0.38 h^{-1}\mathrm{Mpc}$, which agrees well with the offset

---

[5] The dependence of the mean ridgeline colour on magnitude is ignored in this procedure, since for all models the slope in the colour-magnitude relation is very small in the considered colours and magnitude range.

[6] Fragmentation is insignificant in the maxBCG sample, but overmerging slightly boosts the cluster richness estimates mainly due to contamination by foreground and background structures (Koester et al. 2007b).
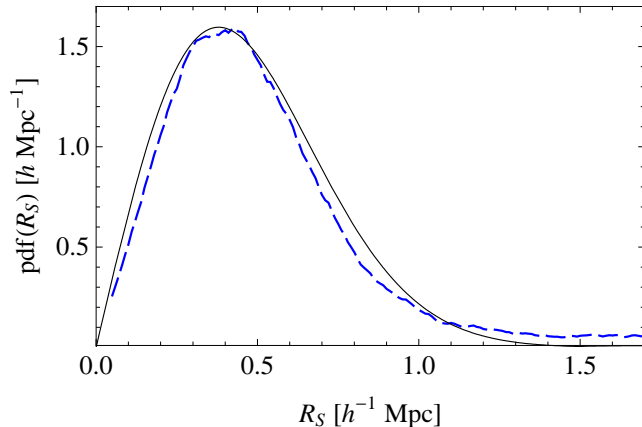
Figure 2. The distribution of projected offset R_s between the 'true' and 'apparent' centres of miscentred clusters in the MS (dashed line). The distribution is well fit by a 2D Gaussian (solid line).

distribution found for the maxBCG algorithm run on simulated data (Johnston et al. 2007b). We find a similar value, $\sigma_s = 0.41h^{-1}$Mpc, for the WMAP1 simulation, and somewhat smaller values, $\sigma_s = 0.34h^{-1}$Mpc, for the WMAP3 simulation.

When needed for our analysis, we will use a probability

$$\tilde{p}_c(N_{\text{int}}^{\text{gal}}) = \frac{1 + 0.04 N_{\text{int}}^{\text{gal}}}{2.2 + 0.05 N_{\text{int}}^{\text{gal}}} \qquad (2)$$

that a cluster in the simulation with $N_{\text{int}}^{\text{gal}}$ ridgeline galaxies is correctly centred. Empirically, this yields roughly the same probability $p_c(N_{200}^{\text{gal}})$ that a cluster with measured richness N_{200}^{gal} is correctly centred as was found for the maxBCG algorithm by Johnston et al. (2007b).

In our simulations, centre misidentification tends to reduce the number N_{200}^{gal} of ridgeline galaxies within R_{200}^{gal} for a given cluster. Consequently, the number density of clusters with N_{200}^{gal} above a given threshold is slightly decreased by centre misidentification. Another consequence of centre misidentification in our simulations is a slightly higher average cluster mass and ridgeline galaxy number $N_{\text{int}}^{\text{gal}}$ for a given measured richness N_{200}^{gal}. All these effects may be smaller for the actual maxBCG algorithm. This algorithm disfavours identifying the cluster centre with galaxies that lead to low N_{200}^{gal} in comparison to galaxies that yield a larger cluster richness. In the following, we will thus discuss results for our simulated cluster samples in the case that centre misidentification is ignored, unless stated otherwise.

2.5 The cluster samples

A comparison of cluster abundances in our simulated cluster samples to observation requires knowledge of the volumes and areas of the real surveys. For the SDSS maxBCG cluster sample, we assume an effective survey area of $7400\,\text{deg}^2$ and a redshift range of $0.1 \leqslant z \leqslant 0.3$ (Rozo et al. 2009b). This yields an effective survey volume of $4.3 \times 10^8 h^{-3}\,\text{Mpc}^3$ for the MS and WMAP1 cosmology, and $4.4 \times 10^8 h^{-3}\,\text{Mpc}^3$ for the WMAP3 cosmology.

For each snapshot of our simulations with redshift $0.1 \leqslant z \leqslant 0.3$, we create a model cluster catalogue containing the

projections of all clusters in the simulation box. We calculate the statistical properties of interest (e.g. the cluster densities or average cluster mass as a function of cluster richness) for each of these snapshot catalogues (properly taking into account the increased cluster number due to inclusion of multiple projections of each cluster). We then compute the properties of a cluster sample in a volume-limited survey with $0.1 \leqslant z \leqslant 0.3$ by an average over the snapshot results, where each snapshot is weighted by its cluster abundance and its volume fraction in the survey.

The simulation cube volume $L^3 = 1.25 \times 10^8 h^{-3}\,\text{Mpc}^3$ for the MS, which is about one quarter of the SDSS maxBCG survey volume. The simulation cube is used in three different projections and at six different redshifts to construct the model cluster samples, which increases the effective sample size.[7] One can thus expect the statistical errors due to sample variance to be roughly the same for the MS model and the SDSS maxBCG cluster sample, and about eight times larger for the WMAP models (with their 64 times smaller box volume).

Where appropriate, we estimate the errors of our models due to sample variance in the following way: We divide the simulation cube of the MS into 64 smaller cubes each having the size of the WMAP simulations. We calculate the observables for each of these subcubes separately. The standard deviation of the results from the different subcubes serves as an estimate for the statistical error of the WMAP1-A model. The statistical errors for the other models are than extrapolated from the WMAP1-A error using simple assumptions about the scaling with volume, numbers, etc.

3 RESULTS

Here, we compare the properties of clusters in our various galaxy formation models to the observed properties of clusters in the SDSS maxBCG catalogue. We investigate average cluster properties as a function of galaxy content by dividing our simulated cluster samples into bins of richness N_{200}^{gal} and luminosity L_{200}^{gal} (as was done for the maxBCG cluster sample). The average properties of the model clusters binned by N_{200}^{gal} are listed for the different galaxy formation models in Tables 7-10. The properties of model clusters when binned by L_{200}^{gal} are shown in Tables 11-14.

We first present results for stacked weak-lensing mass profiles and for the abundance of clusters, both as a function of galaxy richness. We then discuss the mean and scatter of cluster mass as functions of richness and luminosity. Finally, we study how well the cluster mass function and the stacked weak-lensing mass profiles can reconstructed from the cluster abundance together with the mean and scatter of the mass-richness relation.

3.1 Cluster mass profiles

For each cluster in the simulations, we compute weak-lensing mass profiles by projecting the simulation particles and the

---

[7] The resulting effective sample size is difficult to quantify since the subsamples created from the different projections and redshifts are not independent.

galaxies in a cuboid region of $35h^{-1}$ Mpc transverse physical side length and $100h^{-1}$ Mpc comoving thickness centred on the cluster. The projected particles and galaxies (assumed to contribute their stellar mass as points)[8] are binned in annuli to compute the circularly averaged surface mass density $\Sigma(R)$ at radius R from the projected cluster centre, the mean enclosed surface mass density $\bar{\Sigma}(R)$ inside R, and the weak-lensing mass profile

$$\Delta\Sigma(R) = \bar{\Sigma}(R) - \Sigma(R). \tag{3}$$

The weak-lensing mass profile $\Delta\Sigma(R)$ is proportional to the average tangential shear $\langle\gamma_t\rangle(R)$ around the projected cluster centre, and can therefore be measured using weak-lensing observations (Schneider et al. 2006). To increase signal-to-noise, the measured tangential shear may be averaged over a sample of clusters. The resulting shear signal can then be converted to an average mass profile for the observed cluster sample.

In this section, the weak-lensing mass profiles of the simulated clusters in each snapshot are averaged in bins of N_{200}^{gal}. The average profiles from each snaphot are then combined with appropriate weights to obtain a mean profile for each N_{200}^{gal}-bin in a volume-limited survey. In doing this, we also take into account the effect of cluster centre misidentification, which has a considerable impact on the average profiles at radii $R < 1h^{-1}$ Mpc (see Sec. 3.7).

In Fig. 3, the weak-lensing mass profiles for the simulated clusters in the MS and the WMAP models are compared to the measured profiles of maxBCG clusters in the SDSS (Sheldon et al. 2009a). The simulated and observed profiles agree remarkably well in detailed shape and amplitude. This is strong evidence that our models provide a realistic description not only of the density profile and galaxy content of galaxy clusters, but also of the maxBCG cluster selection and richness measurement.

Differences between the galaxy models and the observations are small but noticeable. The simulated density profiles of the MS tend to be above the observed profiles in the poorer clusters but are an excellent fit in the rich systems. The WMAP3 model profiles fit better in the poor clusters but are mostly below the observed profiles in richer clusters. For radii $R \lesssim 1h^{-1}$Mpc, the mass profiles of the WMAP3 models are roughly 30% lower than in the MS/WMAP1 models. This suggests that for given richness, the maxBCG clusters are on average slightly less massive than clusters in the MS/WMAP1 simulations but slightly more massive than those in the WMAP3 simulations. We will investigate this issue in more detail in Sec. 3.3.

3.2 Cluster abundance

Table 3 compares the area density $n_{\geqslant10}^{ang}$ of clusters with richness $N_{200}^{gal} \geqslant 10$ and redshift $0.1 \leqslant z \leqslant 0.3$ in our simulated

---

[8] Although particles in the simulations represent the total mass in the simulated parts of the universe, we do not compensate for the additional stellar mass, since (i) the mass in stars is very small compared to the total mass in collapsed objects, and (ii) gas physics increases the dark-matter density in the inner part of the halos compared to collisionless simulations (e.g. Barnes and White 1984; Gnedin et al. 2004).

Table 3. The area density $n_{\geqslant10}^{ang}$ [in deg^{-2}] of clusters with richness $N_{200}^{gal} \geqslant 10$ and redshift $0.1 \leqslant z \leqslant 0.3$ for the model clusters in the MS and WMAP simulations and for the SDSS maxBCG clusters (Koester et al. 2007a). Considered are the cases that all cluster centres are correctly identified ($p_c = 1$), and that only a fraction of clusters given by Eq. 2 is correctly centred ($p_c < 1$).

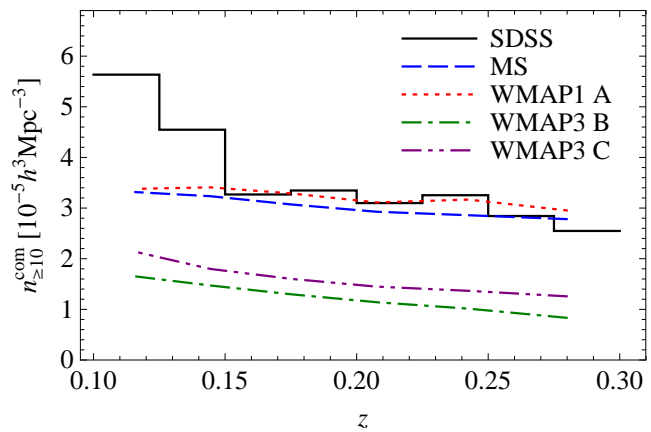|	$p_c = 1$	$p_c < 1$
SDSS		1.8
MS	1.7	1.4
WMAP1-A	1.8	1.6
WMAP3-B	0.6	0.5
WMAP3-C	0.9	0.7

Figure 4. The comoving abundance $n_{\geqslant10}^{com}(z)$ of clusters with richness $N_{200}^{gal} \geqslant 10$ as a function of redshift z in the SDSS maxBCG catalogue (Koester et al. 2007a) and in our simulated cluster catalogues based on the MS and the WMAP simulations.

surveys to the observed abundance of maxBCG clusters in the SDSS. If we ignore misidentification of the cluster centres, the MS and the WMAP1-A model yield cluster abundances very similar to the real maxBCG cluster sample. In contrast, the cluster abundances for the WMAP3 models are a factor 2-3 lower than that observed in the SDSS. The lowest abundance is found for the WMAP3-B model.

To obtain an estimate for the statistical error on the cluster density, we employ the subsampling method described in Sec. 2.5: We use the MS model to create subsamples with sizes equal to the WMAP1-A model. From these subsamples, we estimate a standard deviation for the area density of clusters of 25% for the WMAP1-A model. Taking into account the lower cluster densities in the WMAP3 models, a slightly larger statistical error of 30-40% can be assumed for these. A simple extrapolation of the WMAP1-A error yields a much smaller error of 3% for the cluster density in the MS model.

Taking into account centre misidentification in our simulations reduces the cluster abundances by $\approx$ 20% and thus increases the discrepancy between the WMAP3 models and the SDSS cluster sample. The abundance is then also somewhat low even in the MS case, suggesting, as noted above, that our procedure for modelling the effects of centre misidentification may overestimate the effect in the real maxBCG catalogues.
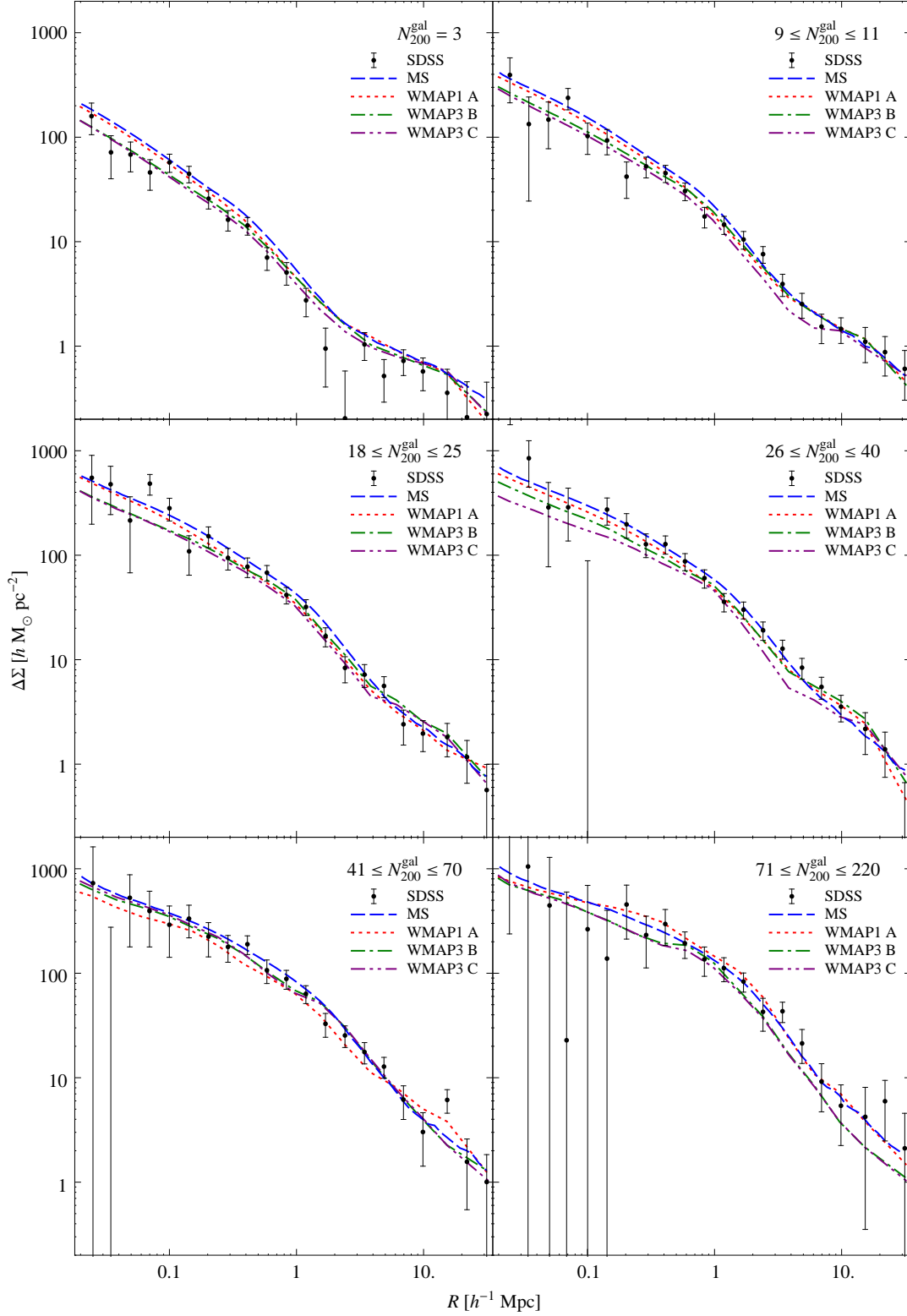
Figure 3. The average weak-lensing mass profile $\Delta\Sigma(R)$ as a function of radius R for clusters in different richness bins in the MS (dashed lines), WMAP1-A (dotted lines), WMAP3-B (dash-dotted lines), and the WMAP3-C model (dash-dot-dotted lines) compared to the observed profiles in the SDSS (Sheldon et al. 2009a, points with error bars).
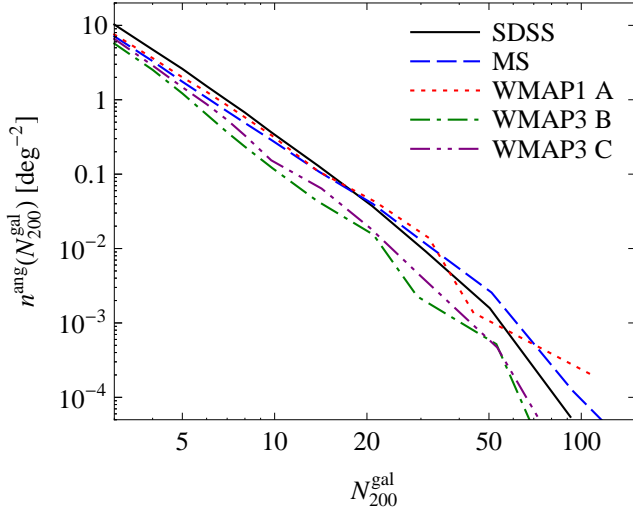
Figure 5. The surface density $n^{\mathrm{ang}}(N_{200}^{\mathrm{gal}})$ of clusters with redshift $0.1 \leqslant z \leqslant 0.3$ as a function of richness N_{200}^{gal}. Counts in the SDSS maxBCG cluster sample (Koester et al. 2007a) are compared to counts in our simulated cluster catalogues for the MS and the WMAP simulations.

The redshift dependence of the comoving cluster abundance is shown in Fig. 4. All our models show a slight decrease of the comoving cluster density with increasing redshift. The statistical errors on the comoving cluster abundance estimated with the subsampling method are similar to the errors on the cluster area density, i.e. 25-40% for the WMAP models and $\sim 3\%$ for the MS. For $z > 0.15$, the abundance in the MS and WMAP1-A model agree very well with the maxBCG results. In contrast, there is a much larger observed density at low redshifts $z < 0.15$, which is not seen in the models and presumably reflects nearby large-scale structure such as the SDSS Great Wall.

The dependence of the cluster counts on richness N_{200}^{gal} is illustrated in Fig. 5. Cluster abundances in the MS and WMAP1-A models are lower than in the SDSS for $N_{200}^{\mathrm{gal}} < 20$, but exceed the observed abundances for $N_{200}^{\mathrm{gal}} \geqslant 20$. Abundances in the WMAP3 models are always lower than in the MS and WMAP1-A model and below the observations. For $N_{200}^{\mathrm{gal}} \geqslant 9$, the cluster abundances in the WMAP3 models are 2-20 times lower than the abundances in the WMAP1-A model and 2-5 times lower than the observed abundances. Hence, the differences are always larger than the statistical errors inferred from the subsampling (which are $\sim$10-100% for the WMAP models and $\sim$1-10% for the MS and SDSS). The differences are largest in the high-N_{200}^{gal} tail of the distribution.

The low cluster abundance for the WMAP3 models in comparison to the MS and WMAP1-A models, in particular for large N_{200}^{gal}, are a reflection of the different cosmologies. Rich clusters have massive dark matter halos, and there are far fewer massive halos in the WMAP3 cosmology than in the WMAP1 cosmology. This is mainly due to the lower value of σ_8. The higher star formation efficiency in the WMAP3 models does not sufficiently enhance the number of bright ridgeline galaxies per unit mass to compensate for the decrease in the number of massive halos. As a result,
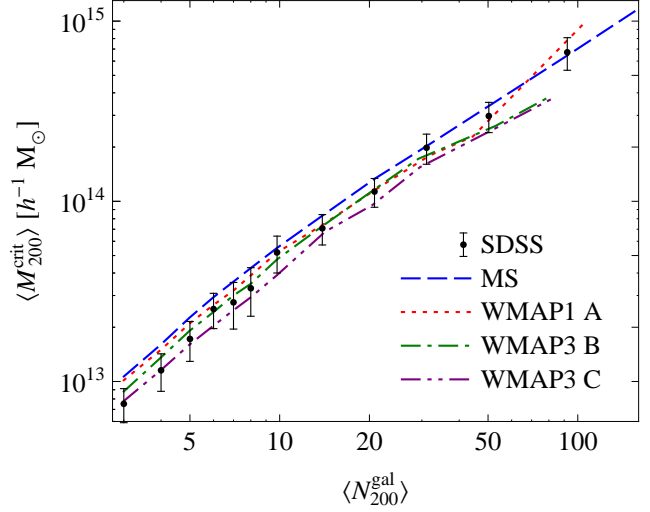

Figure 6. The average cluster mass $\langle M_{200}^{\mathrm{crit}} \rangle$ vs. richness $\langle N_{200}^{\mathrm{gal}} \rangle$ relations for cluster catalogues from the MS and WMAP simulations are compared to the relation derived from the SDSS maxBCG catalogues by Johnston et al. (2007b).

there are fewer rich clusters in the WMAP3 models than in the MS and WMAP1-A models.

The observed abundance of rich clusters is slightly lower than the abundance predicted for the MS and much larger than the abundance predicted by the WMAP3 models. This suggests that $0.72 < \sigma_8 < 0.9$ for our Universe, with σ_8 probably closer to 0.9 than to 0.72. This is consistent with some recent estimates [e.g. $\sigma_8 = 0.80 \pm 0.02$ by Lesgourgues et al. 2007, $\sigma_8 = 0.81 \pm 0.03$ by Komatsu et al. 2009, and $\sigma_8 = (0.83 \pm 0.03)(\Omega_{\mathrm{M}}/0.25)^{-0.41}$ by Rozo et al. 2009b].

The results for the abundances of rich clusters alone are not sufficient to definitely conclude that $0.72 < \sigma_8 < 0.9$. For example, problems with the modelling of the ridgeline galaxies and their identification could have lead to inaccurate estimates for the cluster richness and thus to incorrect cluster abundances. However, there is complementary evidence from the mass-richness relation, which we discuss in Sec. 3.3 and 3.6.

3.3 Mass-richness relation

The weak-lensing mass profiles discussed in Sec. 3.1 can be used to estimate spherical-overdensity cluster masses. This can be done, e.g., by a non-parametric conversion of the weak-lensing mass profiles into average 3D density profiles (Johnston et al. 2007a), or by fitting a parametrised model of the average cluster density to the shear data (Johnston et al. 2007b).

In Fig. 6, average cluster masses $\langle M_{200}^{\mathrm{crit}} \rangle$ in our simulated catalogues[9] are shown as a function of cluster richness $\langle N_{200}^{\mathrm{gal}} \rangle$ and are compared to the corresponding relation for

---

[9] We use the masses measured directly from the matter distribution in the simulations. As discussed in Sec. 3.7, these are consistent with the masses obtained from parametric fits to the weak-lensing mass profiles.
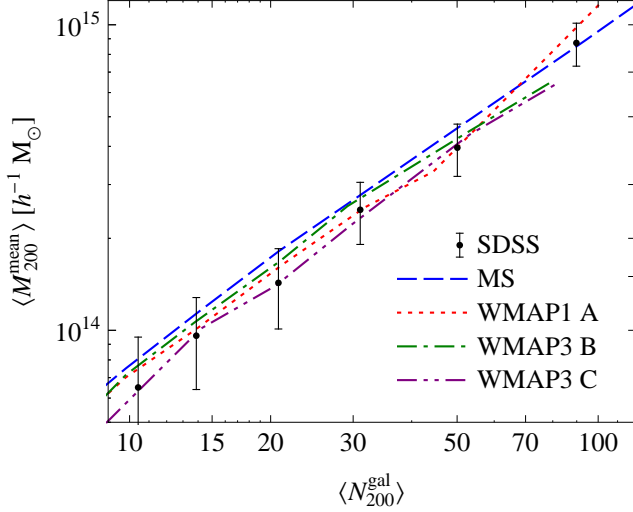
Figure 7. The average cluster mass $\langle M_{200}^{\mathrm{mean}}\rangle$ vs. richness $\langle N_{200}^{\mathrm{gal}}\rangle$ relations for cluster catalogues from our MS and WMAP simulations are compared to the SDSS relation given by Reyes et al. (2008).

SDSS maxBCG clusters by Johnston et al. (2007b), who calculated the cluster masses by fitting parametric models to the observed lensing signal.[10] Remarkably, all our simulations reproduce the observed mass-richness relation within $\sim 30\%$ over the two orders of magnitude spanned by the SDSS clusters. This is corroborates our finding in Sec. 3.1 that our models provide an adequate description of the statistical properties of optically selected galaxy clusters.

At given richness, the differences in cluster density profiles between models and observations (see Fig. 3) imply differences in mean cluster mass. For $N_{200}^{\mathrm{gal}} < 10$, the MS yields cluster masses that are 30-40% higher than the SDSS maxBCG cluster masses derived by Johnston et al. (2007b). For $N_{200}^{\mathrm{gal}} \geqslant 10$, the MS masses are up to 20% higher than the SDSS maxBCG masses. The cluster masses of the WMAP1-A model are comparable to those of the MS, but seem to be affected by sampling noise for large $\langle N_{200}^{\mathrm{gal}}\rangle$. The cluster masses in the WMAP3-B model are lower than those for the MS model by 20-30%, and fall below the SDSS cluster masses at large richness. Among our models, the lowest cluster masses are found for the WMAP3-C model, where the values are always smaller than those in the SDSS.

The mass-richness relation for the WMAP1-A model differs by up to 30% from the relation for the MS model (which is much less affected by sampling noise due to its 64 times larger volume). Using subsamples created from the MS as described in Sec. 2.5, we estimate a standard deviation for the binned cluster mass of 2% for $N_{200}^{\mathrm{gal}} = 3$ and 20% for $71 \leqslant N_{200}^{\mathrm{gal}} \leqslant 220$ for the WMAP1-A model. A similar statistical error can be assumed for the WMAP3 models. This is consistent with the differences between the MS and WMAP1-A models being solely due to sampling noise.

Another analysis of the weak-lensing data for the SDSS

Table 4. The best-fit parameters (calculated from a least-squares fit of $\log_{10}\langle N_{200}^{\mathrm{gal}}\rangle$ against $\log_{10}\langle M_{200}^{\mathrm{crit}}\rangle$) for the mass-richness relation (4) of simulated clusters with $N_{200}^{\mathrm{gal}} \geqslant 9$ is compared to the best-fitting parameters for the SDSS maxBCG clusters with masses measured by Johnston et al. (2007b).

	$M_{200|20}^{\mathrm{crit}}\ [h^{-1}\mathrm{M}_\odot]$	α_N^{crit}
SDSS	$(1.12 \pm 0.03) \times 10^{14}$	1.14 ± 0.04
MS	$(1.24 \pm 0.01) \times 10^{14}$	1.09 ± 0.01
WMAP1-A	$(1.11 \pm 0.08) \times 10^{14}$	1.21 ± 0.09
WMAP3-B	$(1.05 \pm 0.04) \times 10^{14}$	0.97 ± 0.05
WMAP3-C	$(0.92 \pm 0.04) \times 10^{14}$	1.05 ± 0.05

Table 5. The best-fit parameters (calculated from a least-squares fit of $\log_{10}\langle N_{200}^{\mathrm{gal}}\rangle$ against $\log_{10}\langle M_{200}^{\mathrm{mean}}\rangle$) for the mass-richness relation (4) of simulated clusters with $N_{200}^{\mathrm{gal}} \geqslant 9$ is compared to the best-fit parameters for the SDSS maxBCG clusters with masses measured by Reyes et al. (2008).

	$M_{200|20}^{\mathrm{mean}}\ [h^{-1}\mathrm{M}_\odot]$	α_N^{mean}
SDSS	$(1.42 \pm 0.03) \times 10^{14}$	1.19 ± 0.03
MS	$(1.68 \pm 0.02) \times 10^{14}$	1.08 ± 0.01
WMAP1-A	$(1.53 \pm 0.08) \times 10^{14}$	1.19 ± 0.06
WMAP3-B	$(1.58 \pm 0.04) \times 10^{14}$	1.06 ± 0.03
WMAP3-C	$(1.38 \pm 0.04) \times 10^{14}$	1.13 ± 0.04

maxBCG cluster sample has been performed by Reyes et al. (2008). In Fig. 7, we compare the average cluster masses $\langle M_{200}^{\mathrm{mean}}\rangle$ of our simulated clusters to their results as a function of richness. As for $\langle M_{200}^{\mathrm{crit}}\rangle$, the average cluster masses $\langle M_{200}^{\mathrm{mean}}\rangle$ in the MS model are up to 30% larger than the SDSS maxBCG cluster masses, whereas the cluster masses of the WMAP3 models are comparable to those in the SDSS.

The mass-richness relations shown in Fig. 6 and 7 suggest a power law, although with a steeper slope for $\langle N_{200}^{\mathrm{gal}}\rangle < 10$ than for $\langle N_{200}^{\mathrm{gal}}\rangle \gtrsim 10$. Here, we fit the mean mass-richness relation for clusters with $N_{200}^{\mathrm{gal}} \geqslant 9$ by:

$$M_{200}^{\mathrm{crit/mean}}(N_{200}^{\mathrm{gal}}) = M_{200|20}^{\mathrm{crit/mean}} \left(\frac{N_{200}^{\mathrm{gal}}}{20}\right)^{\alpha_N^{\mathrm{crit/mean}}} . \quad (4)$$

The best-fit parameters for our simulated catalogues are compared to those for the SDSS in Tables 4 and 5.

The lower cluster masses in the WMAP3 models than in the MS and WMAP1-A models again reflect the different cosmologies. The less evolved dark matter structure in the WMAP3 cosmology requires more efficient star formation in order to match observed galaxy numbers. This results in more ridgeline galaxies in a dark matter halo of given mass. Consequently, for a given richness, halos are less massive in the WMAP3 models than in the MS and WMAP1-A models.

Except for the largest richness bin, observed cluster masses are smaller than in the MS model. This suggests a normalisation $\sigma_8 < 0.9$ for our Universe (again consistent with the recent estimate $\sigma_8 = 0.81 \pm 0.03$ by Komatsu et al. 2009).

[10] We multiplied the masses given in Johnston et al. (2007b) by a factor 1.18 ± 0.06, which is a photo-z bias correction advocated by Mandelbaum et al. (2008) and Rozo et al. (2009a).
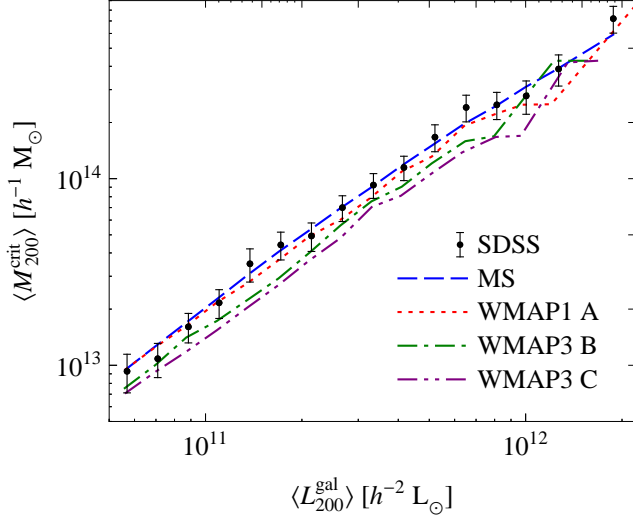
Figure 8. Average cluster mass $\langle M_{200}^{\mathrm{crit}} \rangle$ vs. the total *i*-band luminosity $\langle L_{200}^{\mathrm{gal}} \rangle$ of ridgeline galaxies within R_{200}^{gal}. Results for our MS and WMAP simulations are compared to SDSS results based on cluster masses by Johnston et al. (2007b).

Table 6. The best-fit parameters for the mass-luminosity relation (5) in our simulations (calculated from a least-squares fit of $\log_{10}\langle L_{200}^{\mathrm{gal}} \rangle$ vs. $\log_{10}\langle M_{200}^{\mathrm{crit}} \rangle$) are compared to the values by Johnston et al. (2007b) for the SDSS maxBCG cluster sample.

	$M_{200\mid 40}^{\mathrm{crit}}$ $[h^{-1}\mathrm{M}_\odot]$	α_L^{crit}
SDSS	$(1.09 \pm 0.03) \times 10^{14}$	1.23 ± 0.03
MS	$(1.13 \pm 0.02) \times 10^{14}$	1.18 ± 0.01
WMAP1-A	$(1.00 \pm 0.04) \times 10^{14}$	1.16 ± 0.04
WMAP3-B	$(0.89 \pm 0.02) \times 10^{14}$	1.16 ± 0.02
WMAP3-C	$(0.81 \pm 0.02) \times 10^{14}$	1.17 ± 0.02

3.4 Mass-luminosity relation

The mass-luminosity relation computed by binning our simulated cluster samples in luminosity L_{200}^{gal} is shown in Fig. 8. For given luminosity, the MS model yields cluster masses very similar to the SDSS masses of Johnston et al. (2007b), whereas the WMAP3 model produces mean cluster masses that are generally smaller than the SDSS masses. The best-fit parameters for the mass-luminosity relation

$$M_{200}^{\mathrm{crit}}(L_{200}^{\mathrm{gal}}) = M_{200\mid 40}^{\mathrm{crit}} \left(\frac{L_{200}^{\mathrm{gal}}}{4 \times 10^{11} h^{-2}\mathrm{L}_\odot} \right)^{\alpha_L^{\mathrm{crit}}} \qquad (5)$$

are listed in Table 6.

The differences in the mass-luminosity relation between the various galaxy formation models can be explained in the same way as the differences in the mass-richness relation. The higher star formation efficiency in the WMAP3 models creates more bright ridgeline galaxies in a halo of a given mass M_{200}^{crit} than in the MS and WMAP1-A models. This leads to lower average cluster masses at given luminosity L_{200}^{gal}.
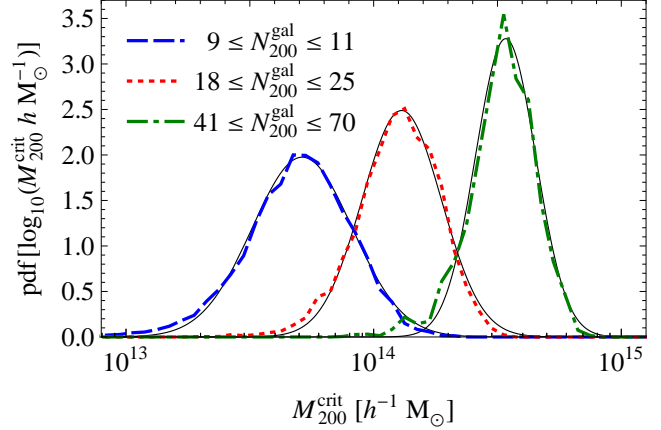

Figure 9. The distribution of the logarithm of cluster mass $\log_{10}(M_{200}^{\mathrm{crit}})$ in various bins of richness N_{200}^{gal}. Shown are distributions for the MS model (dashed/dotted lines) and fits of these distributions to a normal distribution (solid lines).

3.5 The scatter in the mass-richness relation

To compute a cluster mass function from cluster counts and mean masses as a function of richness, one needs to model the scatter in mass at each richness. In Fig. 9, distributions of the logarithm of cluster mass $\log_{10}(M_{200}^{\mathrm{crit}})$ are shown for the MS model for several bins in N_{200}^{gal}. These distributions are well described by gaussians.

For our various galaxy formation models, the standard deviation $\sigma_{\log_{10}(M_{200}^{\mathrm{crit}})}$ of the scatter in the logarithm of cluster mass $\log_{10}(M_{200}^{\mathrm{crit}})$ at given N_{200}^{gal} is listed for various N_{200}^{gal}- and L_{200}^{gal}-bins is in Tables 7-14. The scatter decreases with increasing N_{200}^{gal} or L_{200}^{gal} and tends to be larger at given N_{200}^{gal} than at the corresponding L_{200}^{gal}.

Our values for the scatter in the mass-richness relation are in good agreement with those found empirically by Rozo et al. (2009a) for the maxBCG cluster sample (using X-ray luminosities as an additional mass proxy): We find $\sigma_{\log_{10}(M_{200}^{\mathrm{crit}})} \approx 0.15\text{-}0.2$ for the richness bins with $N_{200}^{\mathrm{gal}} \geqslant 9$, while Rozo et al. (2009a) find $\sigma_{\log_{10}(M_{200}^{\mathrm{crit}})} \approx 0.20 \pm 0.09$ for $N_{200}^{\mathrm{gal}} \approx 40$. Moreover, our values are consistent with the scatter in the velocity dispersion-richness relation derived by Becker et al. (2007) for the maxBCG clusters, if centre misidentification is taken into account. Note that there may be additional effects that increase the observed scatter, but are not modelled here.

3.6 The mass function

When the cluster abundance and the mass distribution at each richness is known, it is straightforward to reconstruct the cluster mass function (Rozo et al. 2009a). The differential cluster number density (or differential mass function) is then given by a sum over all richness bins:

$$\mathrm{d}n(M_{200}^{\mathrm{crit}})/\mathrm{d}M_{200}^{\mathrm{crit}} = \sum_{i=1}^{N_{\mathrm{bins}}} n_i \mathrm{pdf}_i(M_{200}^{\mathrm{crit}}), \qquad (6)$$

where n_i denotes the space density and $\mathrm{pdf}_i(M_{200}^{\mathrm{crit}})$ the mass distribution for clusters in richness bin i.
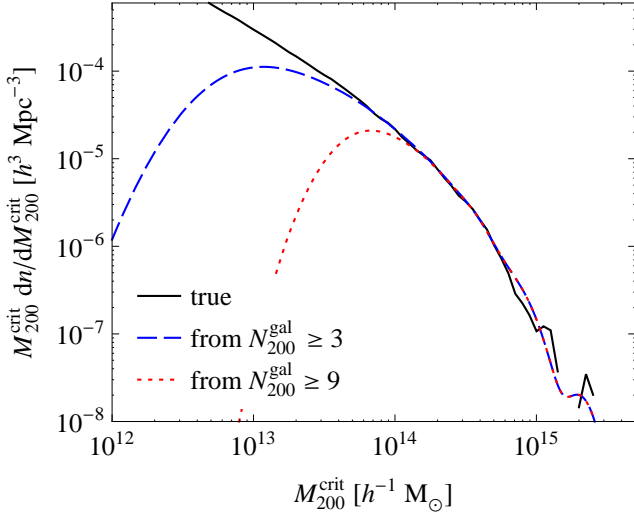
The results of Sec. 3.5 show that the mass distribu-

Figure 10. The differential abundance $\mathrm{d}n(M_{200}^{\mathrm{crit}})/\mathrm{d}M_{200}^{\mathrm{crit}}$ as a function of mass M_{200}^{crit} for clusters with redshift $0.1 \leqslant z \leqslant 0.3$ in the MS: directly measured from the simulation (solid line) and reconstructed from the richness bins with $N_{200}^{\mathrm{gal}} \geqslant 3$ (dashed line) or $N_{200}^{\mathrm{gal}} \geqslant 9$ (dotted line).
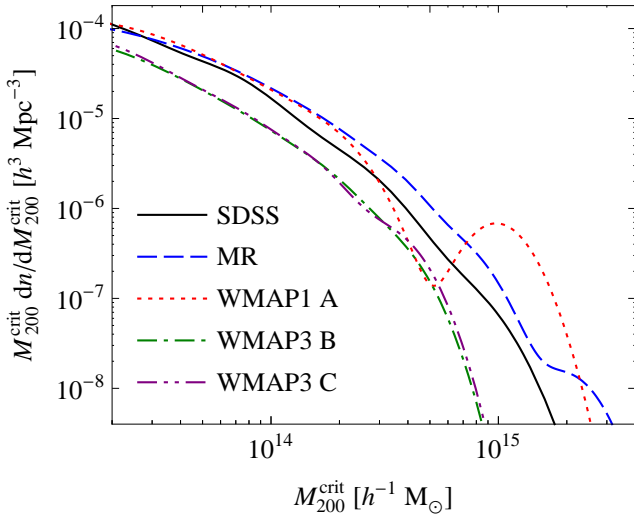

Figure 11. The differential abundance $\mathrm{d}n(M_{200}^{\mathrm{crit}})/\mathrm{d}M_{200}^{\mathrm{crit}}$ as a function of mass M_{200}^{crit} for clusters with redshift $0.1 \leqslant z \leqslant 0.3$ reconstructed from the masses and abundances of clusters with richness $N_{200}^{\mathrm{gal}} \geqslant 3$. Compared are the results for MS and WMAP simulations and the SDSS (calculated from the abundances by Koester et al. 2007a and Sheldon et al. 2009a, the masses by Johnston et al. 2007b, and the scatter by Rozo et al. 2009a).

tions $\mathrm{pdf}_i(M_{200}^{\mathrm{crit}})$ at each richness can be approximated by a log-normal distribution with mean $\langle M_{200}^{\mathrm{crit}} \rangle$ and scatter $\sigma_{\log_{10}(M_{200}^{\mathrm{crit}})}$ given by the values in Table 7-10. As Fig. 10 illustrates for the MS model, the reconstructed mass function matches the true mass function well for $M_{200}^{\mathrm{crit}} \gtrsim 2 \times 10^{14}$. For smaller masses, the richness-selected cluster sample becomes incomplete in mass, and thus the reconstruction fails.

The reconstructed cluster mass functions for the differ-

Figure 12. Comparison of the average weak-lensing mass profiles $\Delta\Sigma(R)$ as a function of radius R for all clusters (solid line), for the correctly centred clusters (dashed line), and for the incorrectly centred clusters (dashed line) in the MS.

ent galaxy models and the SDSS are compared in Fig. 11. The figure illustrates clearly why we expect a ΛCDM cosmology with normalisation $0.72 < \sigma_8 < 0.9$ to provide a better fit to the SDSS cluster data than the models considered here. The values for the WMAP3 models are always much smaller those reconstructed from the SDSS, while the MS yields values above the observations. The reconstructed cluster mass function for the WMAP1 model generally follows the MS results, but is visibly affected by sampling noise for larger cluster masses.

Since the cluster mass function can be recovered from the cluster abundances and cluster masses as functions of richness, these quantities cannot vary independently if the cluster mass function is fixed. Different assumptions about the galaxy formation physics or the richness measurements that, for given richness, lead to higher cluster abundances will also yield lower cluster masses (and vice versa). Thus, the abundance-richness relation discussed in Sec. 3.2 and the mass-richness relation discussed in Sec. 3.3 provide complementary information on the cosmology.

3.7 Fits to the cluster mass profiles

The results of Sec. 3.5 justify the use of a log-normal mass distribution for fits to observed mass profiles (e.g., by Johnston et al. 2007b; Reyes et al. 2008). Here, we illustrate that one can indeed obtain a good fit to the simulated mean mass profiles of clusters with assumptions similar to those used, e.g., by Johnston et al. (2007b).

The mass profiles discussed in Sec. 3.1 are a mixture of correctly and incorrectly centred clusters. In Fig. 12, the simulated average mass profiles of all clusters are compared to the profiles of correctly and incorrectly centred clusters. The profiles agree well for large radii, but differ significantly below a certain radius $R \approx 0.5h^{-1}$ Mpc for clusters with richness $N_{200}^{\mathrm{gal}} = 3$, and $R \approx 1h^{-1}$ Mpc for clusters with $N_{200}^{\mathrm{gal}} \geqslant 9$.

As Fig. 12 illustrates, centre misidentification has a sig-

Figure 13. Fit to the weak-lensing mass profile $\Delta\Sigma(R)$ as a function of radius R of correctly centred clusters in the MS model. Shown are the measured profiles (solid line), the 3-component fit (dashed line), the central galaxy contribution (dash dotted line), the DM halo contribution (dotted line), and the contribution from neighbouring masses (dash-dot-dotted line).
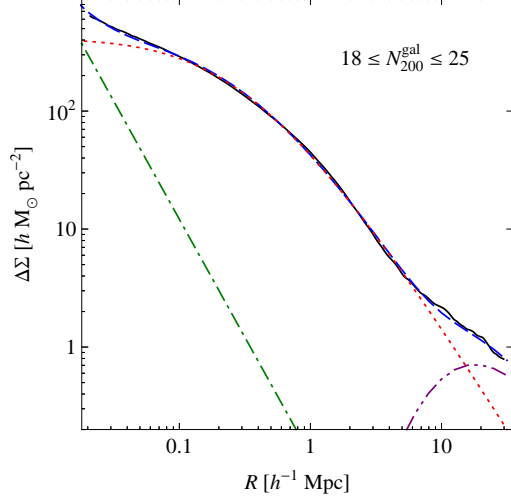

Figure 14. Fit to the weak-lensing mass profile $\Delta\Sigma(R)$ as a function of radius R of incorrectly centred clusters in the MS model. Shown are the measured profiles (solid line), the 4-component fit (short-dashed line), the central galaxy contribution (dash-dotted line), the DM halo contribution (dotted line), the contribution from neighbouring masses (dash-dot-dotted line), and the subhalo contribution (long-dashed line).

nificant impact on the average cluster mass profiles and thus needs to be taken into account in profile fits. Since stacking weak-lensing mass profiles is linear, we can discuss the contributions from correctly and incorrectly centred clusters separately. A weighted average of fits to these two components constitutes a fit to the average mass profile of all clusters in a richness bin.

We assume that the average mass profile of the correctly centred clusters in a richness bin consists of a central galaxy component, which we model as point mass, a mean dark matter halo modelled as an average over spherical NFW profiles (Navarro et al. 1997), and a contribution from neighbouring mass concentrations. A log-normal distribution with mean $\langle M_{200}^{\mathrm{crit}}\rangle$ and standard deviation $\sigma_{log_{10}(M_{200}^{\mathrm{crit}})}$ given by Table 7 is assumed for the halo masses. Furthermore, we assume that the concentration c of halos with mass M_{200}^{crit} follows a log-normal distribution with mean

$$\langle c\rangle\left(M_{200}^{\mathrm{crit}}\right) = 4.67\left(\frac{M_{200}^{\mathrm{crit}}}{10^{14}h^{-1}\mathrm{M_\odot}}\right)^{-0.11} \qquad (7)$$

and standard deviation $\sigma_{\log_{10}(c)} = 0.15$ (Neto et al. 2007).

The resulting fit to the average weak-lensing mass profile of correctly centred clusters is shown in Fig. 13 for clusters in the MS model with richness $18 \leqslant N_{200}^{\mathrm{gal}} \leqslant 25$. A fit of similar quality can also be obtained for the other richness bins.

We now turn to the contribution from incorrectly centred clusters. Figure 12 shows that the average profile of the incorrectly centred clusters increases with decreasing radius even for small radii. This is a consequence of the particular choice for the apparent centre of these clusters in our simulation, namely another massive cluster galaxy within a massive subhalo. If the apparent cluster centres were chosen randomly, one would expect the profile to decrease with decreasing radius for $R < 1h^{-1}\,\mathrm{Mpc}$ (Johnston et al. 2007b).

To obtain a good fit to the average mass profiles of in-

correctly centred clusters, we thus need four components: a central galaxy component (again modelled as point mass), a mean dark matter halo modelled as an NFW profile convolved with a 2D Gaussian, a contribution from neighbouring masses, and a subhalo, which we model as a truncated NFW profile (Baltz et al. 2009). As Fig. 14 illustrates, the subhalo component is essential for a good fit to the simulated mass profiles.

4   SUMMARY AND DISCUSSION

In this work, we have used N-body simulations of cosmic structure formation with semi-analytic galaxy formation modelling to test this modelling and to investigate how the properties of optically selected galaxy groups and clusters depend on cosmological parameters. We have created catalogues of simulated galaxy groups/clusters from model galaxy catalogues (by De Lucia and Blaizot 2007; Wang et al. 2008). We have computed weak-lensing mass profiles and various other properties for these clusters as a function of cluster richness N_{200}^{gal} and luminosity L_{200}^{gal} (as defined by the maxBCG algorithm of Koester et al. 2007b), and compared the results to observations of clusters in the SDSS (Sheldon et al. 2009a; Johnston et al. 2007b; Reyes et al. 2008).

We find that the simulated weak-lensing mass profiles and the observed profiles of the SDSS maxBCG clusters agree remarkably well in detailed shape and amplitude. Moreover, all simulations reproduce the observed mass-richness relation within $\sim 30\%$ over the whole range probed by the SDSS clusters. The MS and the WMAP1-A simulation also yield cluster abundances very similar to the observed abundances. This shows that the models considered here provide a good description of the masses, den-

sity profiles and optical properties of galaxy clusters as well as the optical cluster selection and richness estimation of the maxBCG algorithm. Evidently, using mock galaxy catalogues based on a large high-resolution ΛCDM structure formation simulation and semi-analytic galaxy formation models makes it possible to create very realistic mock cluster catalogues for surveys like the SDSS (when problems with the ridgeline colours are overcome).

Although the underlying N-body simulations assume different cosmological parameters that lead to different DM halo abundances (Springel et al. 2005; Wang et al. 2008), all the galaxy models used here are able to reproduce the observed abundance and two-point correlations of galaxies reasonably well through careful adjustment of their star-formation efficiency and feedback parameters (De Lucia and Blaizot 2007; Wang et al. 2008). They differ, however, in their predicted cluster abundance as a function of $N_{200}^{\rm gal}$. The MS model and the WMAP1-A model, both of which use cosmological parameters based on 1st-year WMAP data (Spergel et al. 2003), predict cluster abundances that are compatible with the observed values (Sheldon et al. 2009a), whereas the WMAP3-A and WMAP3-B models, which use parameters consistent with the WMAP 3rd-year results (Spergel et al. 2007), yield abundances that are lower by a factor 2-3.

The cluster masses predicted as a function of richness $N_{200}^{\rm gal}$ or luminosity $L_{200}^{\rm gal}$ also differ for the different galaxy formation models. At given richness or luminosity, the MS and WMAP1-A models produce clusters that are up to 30% more massive than observed, while the WMAP3 cluster masses are similar to or lower than the observed masses.

The different abundances and average cluster masses in our various galaxy formation models are primarily a reflection of the different underlying cosmologies. Because halos in the WMAP3 cosmology are less massive than in the MS/WMAP1 cosmology, the WMAP3 models need more efficient star formation to match the observed galaxy number densities. This produces more ridgeline galaxies in a dark matter halo of given mass. Consequently, clusters at a given richness are less massive in the WMAP3 models than in the MS and WMAP1-A models. Nevertheless, the higher star formation efficiency in the WMAP3 models does not fully compensate for the lower number of massive halos. So there are fewer rich clusters in the WMAP3 models than in the MS and WMAP1-A models.

The lower cluster masses in the observations compared to the MS model suggests that our Universe would be better described by $\sigma_8 < 0.9$. The higher observed rich cluster abundance than in the WMAP3 models suggests that $\sigma_8 > 0.72$. Thus, more precise agreement between predicted and observed cluster properties is expected for an intermediate value $0.72 < \sigma_8 < 0.9$. This corroborates the findings by Rozo et al. (2009b) that the SDSS maxBCG cluster data favour $\sigma_8 \approx 0.83$.

Our results confirm that the mass distribution of clusters of given richness is well described by a log-normal distribution. This justifies both the assumption of such distributions and the specific scatter values adopted in previous work which modelled stacked cluster mass profiles or reconstructed cluster mass functions. Fits to the stacked mass profile of clusters whose centre has erroneously been identified with a non-central cluster galaxy should take into account a

halo component associated with this non-central galaxy in addition to its stellar mass, the halo component of the main cluster, and surrounding large-scale structure.

Our simulations required many simplifying assumptions about the richness measurements (e.g. about limiting magnitudes, colours, or projection effects), which could result in biased estimates. Although predictions for cluster abundances or for cluster masses are individually subject to such modelling errors, they do not vary independently for varying assumptions about the richness measurement. For example, assuming a fainter magnitude limit results in lower cluster masses *and* higher cluster numbers. Thus, it proves difficult to decrease average cluster masses for MS model in order to better match the observations without producing too many rich clusters. Similarly, the cluster numbers in the WMAP3 models can only be brought into agreement with the observed counts at the cost of cluster masses which are too small.

Similar reasoning reveals that changes to the galaxy formation description alone, though they could change the number, colour, or brightness of the model galaxies, could only lead to better agreement for either cluster abundance or cluster mass, but not both. This stems from the constraint that the abundances and masses of clusters as a function of richness must 'add up' to reproduce the underlying cluster mass function regardless of the specific galaxy formation model. To reach better agreement for both, the number of massive clusters has to be adjusted, too, by changing the cosmology.

Our results demonstrate that, on the one hand, the cluster mass-richness relation and the cluster abundance-richness function together provide strong constraints for the cosmology even without perfect knowledge of the galaxy formation physics. On the other hand, our findings show that the cluster abundance and cluster mass as functions of richness can also be used directly, in addition to galaxy abundance and galaxy two-point correlation, to test the galaxy models.

In future work, one should test how much the agreement between observed and predicted cluster properties can be improved by choosing different cosmological parameters for the simulations (e.g. the values currently favoured by other observations such as Komatsu et al. 2009). In addition, the galaxy models discussed here should be improved to better match the observed colours of ridgeline galaxies at higher redshift. (If we had not adjusted the ridgeline colour selection by hand, the models would have contained almost no clusters with $z > 0.25$.) Future simulations should also probe other cosmologies and galaxy models. These simulations need to have a much larger volume than the WMAP simulations to have good enough statistics to match upcoming observations. (The statistical errors on the mass-richness relation in the WMAP simulations are comparable to the uncertainties in current observations.)

More realistic modelling of cluster selection and characterisation could be achieved by running the observational cluster-finding algorithms on mock galaxy catalogues created from the simulations. Moreover, ray-tracing techniques could be used to simulate realistically the weak-lensing mass measurements and to assess their statistical accuracy and possible systematic uncertainties.

Finally we note that there is some tension between our

finding that the abundances and weak-lensing masses of clusters favour cosmologies with a normalisation $\sigma_8 \approx 0.8$ over those with $\sigma_8 = 0.72$ (in agreement with estimates by Rozo et al. 2009b; Komatsu et al. 2009) and the findings by Li et al. (2009) and Cacciato et al. (2009) that galaxy-galaxy lensing and galaxy clustering data are consistent with $\sigma_8 = 0.73$. It is beyond the scope of this paper to analyse possible reasons for this discrepancy and whether it can be resolved with better handling of measurement systematics or improved structure formation models, but this should be done in future work.

REFERENCES

Baltz E.A., Marshall P., Oguri M., 2009, Journal of Cosmology and Astro-Particle Physics, 1, 15

Barnes J., White S.D.M., 1984, MNRAS, 211, 753

Bartelmann M., Huss A., Colberg J.M., Jenkins A., Pearce F.R., 1998, A&A, 330, 1

Bartelmann M., Doran M., Wetterich C., 2006, A&A, 454, 27

Becker M.R., et al., 2007, ApJ, 669, 905

Bonaldi A., Tormen G., Dolag K., Moscardini L., 2007, MNRAS, 378, 1248

Borgani S., et al., 2001, ApJ, 561, 13

Cacciato M., van den Bosch F.C., More S., Li R., Mo H.J., Yang X., 2009, MNRAS, 394, 929

Colless M., et al., 2003, VizieR Online Data Catalog, 7226, 0

Cooray A., Sheth R., 2002, Phys. Rep., 372, 1

Croton D.J., et al., 2006, MNRAS, 365, 11

Cypriano E.S., Sodré L.J., Kneib J.P., Campusano L.E., 2004, ApJ, 613, 95

De Lucia G., Blaizot J., 2007, MNRAS, 375, 2

De Lucia G., Kauffmann G., White S.D.M., 2004, MNRAS, 349, 1101

De Lucia G., Springel V., White S.D.M., Croton D., Kauffmann G., 2006, MNRAS, 366, 499

Eke V.R., Cole S., Frenk C.S., 1996, MNRAS, 282, 263

Fedeli C., Bartelmann M., Meneghetti M., Moscardini L., 2008, A&A, 486, 35

Francis M.J., Lewis G.F., Linder E.V., 2009, MNRAS, 393, L31

Frenk C.S., White S.D.M., Efstathiou G., Davis M., 1990, ApJ, 351, 10

Gnedin O.Y., Kravtsov A.V., Klypin A.A., Nagai D., 2004, ApJ, 616, 16

Grossi M., Springel V., 2009, MNRAS, 394, 1559

Hansen S.M., McKay T.A., Wechsler R.H., Annis J., Sheldon E.S., Kimball A., 2005, ApJ, 633, 122

Hoekstra H., 2007, MNRAS, 379, 317

Jenkins A., Frenk C.S., White S.D.M., Colberg J.M., Cole S., Evrard A.E., Couchman H.M.P., Yoshida N., 2001, MNRAS, 321, 372

Johnston D.E., Sheldon E.S., Tasitsiomi A., Frieman J.A., Wechsler R.H., McKay T.A., 2007a, ApJ, 656, 27

Johnston D.E., et al., 2007b, ArXiv e-prints, arXiv:0709.1159

Kauffmann G., Colberg J.M., Diaferio A., White S.D.M., 1999, MNRAS, 303, 188

Kitzbichler M.G., White S.D.M., 2007, MNRAS, 376, 2

Kochanek C.S., White M., Huchra J., Macri L., Jarrett T.H., Schneider S.E., Mader J., 2003, ApJ, 585, 161

Koester B.P., et al., 2007a, ApJ, 660, 239

Koester B.P., et al., 2007b, ApJ, 660, 221

Komatsu E., et al., 2009, ApJS, 180, 330

Lesgourgues J., Viel M., Haehnelt M.G., Massey R., 2007, Journal of Cosmology and Astro-Particle Physics, 11, 8

Li R., Mo H.J., Fan Z., Cacciato M., van den Bosch F.C., Yang X., More S., 2009, MNRAS, 394, 1016

Lukić Z., Heitmann K., Habib S., Bashinsky S., Ricker P.M., 2007, ApJ, 671, 1160

Mandelbaum R., et al., 2008, MNRAS, 386, 781

Navarro J.F., Frenk C.S., White S.D.M., 1997, ApJ, 490, 493

Neto A.F., et al., 2007, MNRAS, 381, 1450

Piffaretti R., Valdarnini R., 2008, A&A, 491, 71

Press W.H., Schechter P., 1974, ApJ, 187, 425

Reiprich T.H., Böhringer H., 2002, ApJ, 567, 716

Reyes R., Mandelbaum R., Hirata C., Bahcall N., Seljak U., 2008, MNRAS, 390, 1157

Rines K., Geller M.J., Kurtz M.J., Diaferio A., 2003, AJ, 126, 2152

Rozo E., et al., 2009a, ApJ, 699, 768

Rozo E., et al., 2009b, ArXiv e-prints, arXiv:0902.3702

Schneider P., Kochanek C., Wambsganss J., 2006, *Gravitational Lensing: Strong, Weak and Micro*, Saas-Fee Advanced Course 33, Springer, Berlin

Schulz A.E., White M., 2003, ApJ, 586, 723

Sheldon E.S., et al., 2009a, ApJ, 703, 2217

Sheldon E.S., et al., 2009b, ApJ, 703, 2232

Sheth R.K., Tormen G., 1999, MNRAS, 308, 119

Spergel D.N., et al., 2003, ApJS, 148, 175

Spergel D.N., et al., 2007, ApJS, 170, 377

Springel V., 2005, MNRAS, 364, 1105

Springel V., White S.D.M., Tormen G., Kauffmann G., 2001, MNRAS, 328, 726

Springel V., et al., 2005, Nature, 435, 629

Stanek R., Evrard A.E., Böhringer H., Schuecker P., Nord B., 2006, ApJ, 648, 956

Staniszewski Z., et al., 2009, ApJ, 701, 32

Tyson J.A., Wenk R.A., Valdes F., 1990, ApJ, 349, L1

Vikhlinin A., et al., 2009, ApJ, 692, 1060

Voit G.M., 2005, Reviews of Modern Physics, 77, 207

Wambsganss J., Bode P., Ostriker J.P., 2004, ApJ, 606, L93

Wang J., De Lucia G., Kitzbichler M.G., White S.D.M., 2008, MNRAS, 384, 1301

Warren M.S., Abazajian K., Holz D.E., Teodoro L., 2006, ApJ, 646, 881

Weinmann S.M., van den Bosch F.C., Yang X., Mo H.J.,
 Croton D.J., Moore B., 2006, MNRAS, 372, 1161
White M., Hernquist L., Springel V., 2002, ApJ, 579, 16
Zwicky F., 1937, ApJ, 86, 217

Table 7. The average properties of the model clusters in the MS as inferred from the galaxy model by De Lucia and Blaizot (2007) in bins of richness $N_{200}^{\rm gal}$: the comoving number density n, the average number $\langle N_{\rm int}^{\rm gal} \rangle$ of ridgeline galaxies, the average number $\langle N_{200}^{\rm gal} \rangle$ of ridgeline galaxies within $R_{200}^{\rm gal}$, the average cluster radius $\langle R_{200}^{\rm gal} \rangle$, the average ridgeline i-band luminosity $\langle L_{200}^{\rm gal} \rangle$ within $R_{200}^{\rm gal}$, the average cluster masses $\langle M_{200}^{\rm crit} \rangle$, and the standard deviation $\sigma_{\log_{10}(M_{200}^{\rm crit})}$ of the logarithmic cluster mass. For bins containing < 7 independent clusters, $\sigma_{\log_{10}(M_{200}^{\rm crit})}$ is omitted.

bin	$N_{200}^{\rm gal}$	$n\ [h^3{\rm Mpc}^{-3}]$	$\langle N_{\rm int}^{\rm gal} \rangle$	$\langle N_{200}^{\rm gal} \rangle$	$\langle R_{200}^{\rm gal} \rangle\ [h^{-1}{\rm Mpc}]$	$\langle L_{200}^{\rm gal} \rangle\ [h^{-1}{\rm L}_\odot]$	$\langle M_{200}^{\rm crit} \rangle\ [h^{-1}{\rm M}_\odot]$	$\sigma_{\log_{10}(M_{200}^{\rm crit})}$
1	3	1.2×10^{-4}	2.7	3.0	0.37	5.9×10^{10}	1.1×10^{13}	0.32
2	4	5.6×10^{-5}	3.6	4.0	0.45	8.0×10^{10}	1.6×10^{13}	0.31
3	5	3.0×10^{-5}	4.6	5.0	0.52	1.0×10^{11}	2.3×10^{13}	0.28
4	6	1.8×10^{-5}	5.7	6.0	0.58	1.2×10^{11}	2.9×10^{13}	0.26
5	7	1.2×10^{-5}	6.7	7.0	0.64	1.5×10^{11}	3.6×10^{13}	0.24
6	8	8.3×10^{-6}	7.7	8.0	0.69	1.7×10^{11}	4.3×10^{13}	0.23
7	9-11	1.4×10^{-5}	9.5	9.8	0.78	2.1×10^{11}	5.5×10^{13}	0.21
8	12-17	1.1×10^{-5}	13.7	14.0	0.95	2.9×10^{11}	8.4×10^{13}	0.19
9	18-25	5.4×10^{-6}	20.7	20.9	1.18	4.3×10^{11}	1.3×10^{14}	0.17
10	26-40	3.0×10^{-6}	30.6	31.2	1.44	6.4×10^{11}	2.0×10^{14}	0.15
11	41-70	1.3×10^{-6}	48.9	51.0	1.81	1.0×10^{12}	3.4×10^{14}	0.14
12	71-220	3.3×10^{-7}	86.6	93.8	2.36	1.9×10^{12}	6.6×10^{14}	0.15
13	221-660	1.1×10^{-8}	235.5	269.1	3.69	5.1×10^{12}	2.1×10^{15}	–

Table 8. The properties of the cluster sample in the WMAP1-A model in bins of richness $N_{200}^{\rm gal}$ (see Table 7 for a description of the listed quantities).

bin	$N_{200}^{\rm gal}$	$n\ [h^3{\rm Mpc}^{-3}]$	$\langle N_{\rm int}^{\rm gal} \rangle$	$\langle N_{200}^{\rm gal} \rangle$	$\langle R_{200}^{\rm gal} \rangle\ [h^{-1}{\rm Mpc}]$	$\langle L_{200}^{\rm gal} \rangle\ [h^{-1}{\rm L}_\odot]$	$\langle M_{200}^{\rm crit} \rangle\ [h^{-1}{\rm M}_\odot]$	$\sigma_{\log_{10}(M_{200}^{\rm crit})}$
1	3	1.3×10^{-4}	2.7	3.0	0.37	6.0×10^{10}	1.0×10^{13}	0.32
2	4	6.2×10^{-5}	3.6	4.0	0.45	8.1×10^{10}	1.5×10^{13}	0.30
3	5	3.4×10^{-5}	4.7	5.0	0.52	1.0×10^{11}	2.1×10^{13}	0.26
4	6	2.2×10^{-5}	5.8	6.0	0.58	1.2×10^{11}	2.7×10^{13}	0.24
5	7	1.4×10^{-5}	6.8	7.0	0.64	1.4×10^{11}	3.2×10^{13}	0.22
6	8	9.9×10^{-6}	7.8	8.0	0.69	1.7×10^{11}	3.9×10^{13}	0.22
7	9-11	1.7×10^{-5}	9.4	9.8	0.77	2.1×10^{11}	5.2×10^{13}	0.22
8	12-17	1.1×10^{-5}	13.5	13.8	0.94	2.9×10^{11}	7.3×10^{13}	0.19
9	18-25	5.8×10^{-6}	22.1	21.3	1.20	4.3×10^{11}	1.2×10^{14}	0.16
10	26-40	3.6×10^{-6}	30.9	31.8	1.46	6.6×10^{11}	1.8×10^{14}	0.16
11	41-70	7.9×10^{-7}	40.2	44.5	1.71	8.9×10^{11}	2.3×10^{14}	–
12	71-220	5.1×10^{-7}	94.4	108.1	2.49	2.1×10^{12}	1.0×10^{15}	–

Table 9. The properties of the cluster sample in the WMAP3-B model in bins of richness $N_{200}^{\rm gal}$ (see Table 7 for a description of the listed quantities).

bin	$N_{200}^{\rm gal}$	$n\ [h^3{\rm Mpc}^{-3}]$	$\langle N_{\rm int}^{\rm gal} \rangle$	$\langle N_{200}^{\rm gal} \rangle$	$\langle R_{200}^{\rm gal} \rangle\ [h^{-1}{\rm Mpc}]$	$\langle L_{200}^{\rm gal} \rangle\ [h^{-1}{\rm L}_\odot]$	$\langle M_{200}^{\rm crit} \rangle\ [h^{-1}{\rm M}_\odot]$	$\sigma_{\log_{10}(M_{200}^{\rm crit})}$
1	3	9.6×10^{-5}	2.7	3.0	0.37	5.9×10^{10}	8.8×10^{12}	0.33
2	4	4.2×10^{-5}	3.6	4.0	0.44	8.2×10^{10}	1.4×10^{13}	0.33
3	5	2.0×10^{-5}	4.6	5.0	0.51	1.0×10^{11}	1.9×10^{13}	0.29
4	6	1.1×10^{-5}	5.7	6.0	0.58	1.3×10^{11}	2.4×10^{13}	0.27
5	7	6.2×10^{-6}	6.9	7.0	0.64	1.5×10^{11}	3.0×10^{13}	0.26
6	8	3.9×10^{-6}	7.9	8.0	0.70	1.7×10^{11}	3.5×10^{13}	0.24
7	9-11	6.3×10^{-6}	9.8	9.8	0.79	2.2×10^{11}	4.8×10^{13}	0.25
8	12-17	4.7×10^{-6}	14.6	13.7	0.94	3.0×10^{11}	7.2×10^{13}	0.20
9	18-25	2.2×10^{-6}	21.5	21.0	1.18	4.6×10^{11}	1.2×10^{14}	–
10	26-40	6.6×10^{-7}	33.8	29.2	1.36	6.3×10^{11}	1.7×10^{14}	–
11	41-70	3.0×10^{-7}	64.4	52.9	1.74	1.1×10^{12}	2.6×10^{14}	–
12	71-220	1.6×10^{-7}	72.6	80.4	2.03	1.5×10^{12}	3.8×10^{14}	–

Table 10. The properties of the cluster sample in the WMAP3-C model in bins of richness N_{200}^{gal} (see Table 7 for a description of the listed quantities).

bin	N_{200}^{gal}	$n\ [h^3\mathrm{Mpc}^{-3}]$	$\langle N_{\mathrm{int}}^{\mathrm{gal}}\rangle$	$\langle N_{200}^{\mathrm{gal}}\rangle$	$\langle R_{200}^{\mathrm{gal}}\rangle\ [h^{-1}\mathrm{Mpc}]$	$\langle L_{200}^{\mathrm{gal}}\rangle\ [h^{-1}\mathrm{L}_\odot]$	$\langle M_{200}^{\mathrm{crit}}\rangle\ [h^{-1}\mathrm{M}_\odot]$	$\sigma_{\log_{10}(M_{200}^{\mathrm{crit}})}$
1	3	1.1×10^{-4}	2.6	3.0	0.37	5.8×10^{10}	7.8×10^{12}	0.33
2	4	4.9×10^{-5}	3.6	4.0	0.44	7.9×10^{10}	1.2×10^{13}	0.32
3	5	2.5×10^{-5}	4.6	5.0	0.52	1.0×10^{11}	1.6×10^{13}	0.28
4	6	1.5×10^{-5}	5.6	6.0	0.58	1.2×10^{11}	2.0×10^{13}	0.26
5	7	9.1×10^{-6}	6.5	7.0	0.63	1.4×10^{11}	2.5×10^{13}	0.24
6	8	5.6×10^{-6}	7.3	8.0	0.68	1.7×10^{11}	2.9×10^{13}	0.24
7	9-11	7.9×10^{-6}	9.3	9.7	0.77	2.1×10^{11}	3.9×10^{13}	0.24
8	12-17	6.6×10^{-6}	14.6	14.2	0.97	3.1×10^{11}	6.8×10^{13}	0.19
9	18-25	2.6×10^{-6}	20.4	20.5	1.16	4.3×10^{11}	9.5×10^{13}	0.20
10	26-40	1.2×10^{-6}	30.1	29.6	1.41	6.5×10^{11}	1.5×10^{14}	–
11	41-70	2.5×10^{-7}	65.7	53.2	1.77	1.1×10^{12}	2.5×10^{14}	–
12	71-220	2.7×10^{-7}	77.5	82.0	2.09	1.6×10^{12}	3.7×10^{14}	–

Table 11. The average properties of the model clusters in the MS model in bins of luminosity L_{200}^{gal} (see Table 7 for a description of the listed quantities).

bin	$L_{200}^{\mathrm{gal}}\ [10^{10}h^{-2}\mathrm{L}_\odot]$	$n\ [h^3\mathrm{Mpc}^{-3}]$	$\langle N_{\mathrm{int}}^{\mathrm{gal}}\rangle$	$\langle N_{200}^{\mathrm{gal}}\rangle$	$\langle R_{200}^{\mathrm{gal}}\rangle\ [h^{-1}\mathrm{Mpc}]$	$\langle L_{200}^{\mathrm{gal}}\rangle\ [h^{-1}\mathrm{L}_\odot]$	$\langle M_{200}^{\mathrm{crit}}\rangle\ [h^{-1}\mathrm{M}_\odot]$	$\sigma_{\log_{10}(M_{200}^{\mathrm{crit}})}$
1	5.00 - 6.24	4.1×10^{-5}	2.9	3.3	0.39	5.6×10^{10}	1.0×10^{13}	0.27
2	5.24 - 7.80	4.4×10^{-5}	3.3	3.6	0.42	7.0×10^{10}	1.3×10^{13}	0.27
3	7.80 - 9.74	3.9×10^{-5}	3.8	4.1	0.46	8.7×10^{10}	1.8×10^{13}	0.27
4	9.74 - 12.2	3.1×10^{-5}	4.6	4.9	0.51	1.1×10^{11}	2.4×10^{13}	0.26
5	12.2 - 15.2	2.2×10^{-5}	5.7	5.9	0.58	1.4×10^{11}	3.2×10^{13}	0.24
6	15.2 - 19.0	1.6×10^{-5}	7.2	7.4	0.66	1.7×10^{11}	4.2×10^{13}	0.21
7	19.0 - 23.7	1.1×10^{-5}	9.2	9.3	0.76	2.1×10^{11}	5.6×10^{13}	0.19
8	27.7 - 29.6	7.7×10^{-6}	11.7	11.8	0.87	2.6×10^{11}	7.4×10^{13}	0.18
9	29.6 - 36.9	5.2×10^{-6}	14.9	15.0	0.99	3.3×10^{11}	9.5×10^{13}	0.16
10	36.9 - 46.1	3.7×10^{-6}	18.7	18.9	1.12	4.1×10^{11}	1.2×10^{14}	0.16
11	46.1 - 57.6	2.5×10^{-6}	23.7	23.8	1.26	5.1×10^{11}	1.6×10^{14}	0.15
12	57.6 - 71.9	1.6×10^{-6}	29.3	29.8	1.40	6.4×10^{11}	2.0×10^{14}	0.13
13	71.9 - 89.8	9.6×10^{-7}	37.0	37.9	1.57	8.0×10^{11}	2.6×10^{14}	0.13
14	89.8 - 112.1	6.5×10^{-7}	46.7	47.5	1.76	1.0×10^{12}	3.3×10^{14}	0.12
15	112.1 - 140	4.1×10^{-7}	56.8	59.7	1.94	1.2×10^{12}	4.1×10^{14}	0.13
16	140 - 450	3.6×10^{-7}	84.7	91.2	2.31	1.9×10^{12}	6.4×10^{14}	0.16

Table 12. The average properties of the model clusters in the WMAP1-A model in bins of luminosity L_{200}^{gal} (see Table 7 for a description of the listed quantities).

bin	L_{200}^{gal} $[10^{10}h^{-2}\mathrm{L}_\odot]$	n $[h^3\mathrm{Mpc}^{-3}]$	$\langle N_{\mathrm{int}}^{\mathrm{gal}}\rangle$	$\langle N_{200}^{\mathrm{gal}}\rangle$	$\langle R_{200}^{\mathrm{gal}}\rangle$ $[h^{-1}\mathrm{Mpc}]$	$\langle L_{200}^{\mathrm{gal}}\rangle$ $[h^{-1}\mathrm{L}_\odot]$	$\langle M_{200}^{\mathrm{crit}}\rangle$ $[h^{-1}\mathrm{M}_\odot]$	$\sigma_{\log_{10}(M_{200}^{\mathrm{crit}})}$
1	5.00 - 6.24	4.4×10^{-5}	2.9	3.3	0.39	5.6×10^{10}	9.8×10^{12}	0.27
2	5.24 - 7.80	5.0×10^{-5}	3.2	3.6	0.42	7.0×10^{10}	1.3×10^{13}	0.26
3	7.80 - 9.74	4.4×10^{-5}	3.9	4.2	0.46	8.7×10^{10}	1.7×10^{13}	0.26
4	9.74 - 12.2	3.7×10^{-5}	4.7	5.0	0.52	1.1×10^{11}	2.2×10^{13}	0.24
5	12.2 - 15.2	2.5×10^{-5}	5.6	5.9	0.57	1.4×10^{11}	2.8×10^{13}	0.22
6	15.2 - 19.0	1.7×10^{-5}	7.2	7.2	0.65	1.7×10^{11}	3.8×10^{13}	0.21
7	19.0 - 23.7	1.2×10^{-5}	9.1	9.2	0.75	2.1×10^{11}	5.0×10^{13}	0.19
8	27.7 - 29.6	9.3×10^{-6}	11.4	11.5	0.85	2.6×10^{11}	6.6×10^{13}	0.17
9	29.6 - 36.9	5.9×10^{-6}	14.9	14.5	0.97	3.3×10^{11}	8.5×10^{13}	0.17
10	36.9 - 46.1	4.3×10^{-6}	21.0	19.8	1.15	4.1×10^{11}	1.1×10^{14}	0.15
11	46.1 - 57.6	2.5×10^{-6}	22.8	24.0	1.26	5.1×10^{11}	1.3×10^{14}	–
12	57.6 - 71.9	1.4×10^{-6}	29.2	30.4	1.42	6.5×10^{11}	1.8×10^{14}	–
13	71.9 - 89.8	1.7×10^{-6}	36.2	37.6	1.59	8.0×10^{11}	2.2×10^{14}	–
14	89.8 - 112.1	3.9×10^{-7}	39.4	43.5	1.65	9.6×10^{11}	2.3×10^{14}	–
15	112.1 - 140	1.8×10^{-7}	55.0	63.9	1.88	1.2×10^{12}	2.3×10^{14}	–
16	140 - 450	5.1×10^{-7}	94.5	108.1	2.50	2.1×10^{12}	1.0×10^{15}	–

Table 13. The average properties of the model clusters in the WMAP3-B model in bins of luminosity L_{200}^{gal} (see Table 7 for a description of the listed quantities).

bin	L_{200}^{gal} $[10^{10}h^{-2}\mathrm{L}_\odot]$	n $[h^3\mathrm{Mpc}^{-3}]$	$\langle N_{\mathrm{int}}^{\mathrm{gal}}\rangle$	$\langle N_{200}^{\mathrm{gal}}\rangle$	$\langle R_{200}^{\mathrm{gal}}\rangle$ $[h^{-1}\mathrm{Mpc}]$	$\langle L_{200}^{\mathrm{gal}}\rangle$ $[h^{-1}\mathrm{L}_\odot]$	$\langle M_{200}^{\mathrm{crit}}\rangle$ $[h^{-1}\mathrm{M}_\odot]$	$\sigma_{\log_{10}(M_{200}^{\mathrm{crit}})}$
1	5.00 - 6.24	3.0×10^{-5}	2.8	3.3	0.39	5.6×10^{10}	8.5×10^{12}	0.29
2	5.24 - 7.80	3.2×10^{-5}	3.2	3.6	0.41	7.0×10^{10}	1.1×10^{13}	0.29
3	7.80 - 9.74	3.0×10^{-5}	3.8	4.0	0.45	8.7×10^{10}	1.5×10^{13}	0.29
4	9.74 - 12.2	2.1×10^{-5}	4.4	4.6	0.49	1.1×10^{11}	1.9×10^{13}	0.27
5	12.2 - 15.2	1.4×10^{-5}	5.3	5.4	0.54	1.4×10^{11}	2.4×10^{13}	0.26
6	15.2 - 19.0	8.9×10^{-6}	6.8	6.8	0.63	1.7×10^{11}	3.3×10^{13}	0.24
7	19.0 - 23.7	5.1×10^{-6}	8.9	8.7	0.74	2.1×10^{11}	4.2×10^{13}	0.22
8	27.7 - 29.6	3.7×10^{-6}	11.2	10.8	0.83	2.6×10^{11}	5.9×10^{13}	0.22
9	29.6 - 36.9	2.6×10^{-6}	14.0	13.6	0.93	3.3×10^{11}	7.5×10^{13}	–
10	36.9 - 46.1	1.8×10^{-6}	18.4	17.5	1.06	4.1×10^{11}	1.0×10^{14}	–
11	46.1 - 57.6	9.6×10^{-7}	25.5	22.2	1.22	5.1×10^{11}	1.4×10^{14}	–
12	57.6 - 71.9	5.0×10^{-7}	30.2	26.2	1.32	6.4×10^{11}	1.6×10^{14}	–
13	71.9 - 89.8	2.6×10^{-7}	43.8	35.4	1.45	7.9×10^{11}	2.1×10^{14}	–
14	89.8 - 112.1	1.5×10^{-7}	59.7	49.1	1.68	1.0×10^{12}	2.3×10^{14}	–
15	112.1 - 140	1.3×10^{-7}	67.9	61.4	1.85	1.2×10^{12}	2.9×10^{14}	–
16	140 - 450	1.4×10^{-7}	72.6	81.3	2.03	1.5×10^{12}	3.8×10^{14}	–

Table 14. The average properties of the model clusters in the WMAP3-C model in bins of luminosity L_{200}^{gal} (see Table 7 for a description of the listed quantities).

bin	L_{200}^{gal} $[10^{10}h^{-2}\mathrm{L}_\odot]$	n $[h^3\mathrm{Mpc}^{-3}]$	$\langle N_{\mathrm{int}}^{\mathrm{gal}}\rangle$	$\langle N_{200}^{\mathrm{gal}}\rangle$	$\langle R_{200}^{\mathrm{gal}}\rangle$ $[h^{-1}\mathrm{Mpc}]$	$\langle L_{200}^{\mathrm{gal}}\rangle$ $[h^{-1}\mathrm{L}_\odot]$	$\langle M_{200}^{\mathrm{crit}}\rangle$ $[h^{-1}\mathrm{M}_\odot]$	$\sigma_{\log_{10}(M_{200}^{\mathrm{crit}})}$
1	5.00 - 6.24	3.9×10^{-5}	2.9	3.3	0.39	5.6×10^{10}	8.1×10^{12}	0.29
2	5.24 - 7.80	3.9×10^{-5}	3.3	3.6	0.42	7.0×10^{10}	1.0×10^{13}	0.30
3	7.80 - 9.74	3.3×10^{-5}	3.8	4.1	0.46	8.7×10^{10}	1.3×10^{13}	0.29
4	9.74 - 12.2	2.6×10^{-5}	4.5	4.8	0.50	1.1×10^{11}	1.7×10^{13}	0.27
5	12.2 - 15.2	1.6×10^{-5}	5.5	5.9	0.56	1.4×10^{11}	2.2×10^{13}	0.24
6	15.2 - 19.0	1.0×10^{-5}	6.7	7.0	0.63	1.7×10^{11}	2.9×10^{13}	0.23
7	19.0 - 23.7	6.2×10^{-6}	8.8	8.8	0.73	2.1×10^{11}	3.8×10^{13}	0.21
8	27.7 - 29.6	4.7×10^{-6}	11.6	11.7	0.86	2.6×10^{11}	5.3×10^{13}	0.20
9	29.6 - 36.9	3.5×10^{-6}	14.9	15.0	0.99	3.3×10^{11}	6.9×10^{13}	0.17
10	36.9 - 46.1	2.1×10^{-6}	18.3	17.9	1.09	4.1×10^{11}	9.3×10^{13}	−
11	46.1 - 57.6	1.1×10^{-6}	23.3	23.2	1.24	5.1×10^{11}	1.3×10^{14}	−
12	57.6 - 71.9	6.4×10^{-7}	31.2	27.9	1.38	6.4×10^{11}	1.5×10^{14}	−
13	71.9 - 89.8	3.7×10^{-7}	37.9	33.9	1.49	7.8×10^{11}	1.8×10^{14}	−
14	89.8 - 112.1	1.4×10^{-7}	57.8	48.0	1.70	1.0×10^{12}	2.2×10^{14}	−
15	112.1 - 140	1.4×10^{-7}	67.5	59.7	1.87	1.2×10^{12}	2.7×10^{14}	−
16	140 - 450	2.8×10^{-7}	77.3	81.1	2.07	1.6×10^{12}	3.7×10^{14}	−